ELSEVIER

Journal of Fluids and Structures 23 (2007) 269–295

JOURNAL OF
FLUIDS AND
STRUCTURES

www.elsevier.com/locate/jfs

Time-dependent hydroelastic analysis of cavitating propulsors

Y.L. Young*

Department of Civil and Environmental Engineering, Princeton University, Princeton, NJ 08544, USA

Received 15 August 2005; accepted 3 September 2006
Available online 15 November 2006

Abstract

A 3-D potential-based boundary element method (BEM) is coupled with a 3-D finite element method (FEM) for the time-dependent hydroelastic analysis of cavitating propulsors. The BEM is applied to evaluate the moving cavity boundaries and fluctuating pressures, as well as the added mass and hydrodynamic damping matrices. The FEM is applied to analyze the dynamic blade deformations and stresses due to pressure fluctuations and centrifugal forces. The added mass and hydrodynamic damping matrices are superimposed onto the structural mass and damping matrices, respectively, to account for the effect of fluid–structure interaction. The problem is solved in the time-domain using an implicit time integration scheme. An overview of the formulation for both the BEM and FEM is presented, as well as the BEM/FEM coupling algorithm. Numerical and experiment validation studies are shown. The effects of fluid–structure interaction on the propeller performance are discussed.

Keywords: Fluid–structure interaction; Hydroelastic; Cavitation; Propeller

1. Introduction

Marine propellers usually operate in nonuniform wake due to the hull geometry, shaft inclination, unsteady sea condition, or maneuvering of the ship. Thus, the hydrodynamic blade load, cavitation pattern, and resulting blade stresses change with the blade angle. In addition, the hydrodynamic and centrifugal forces may result in blade deformation, which will in turn affect the surrounding flow field. Nevertheless, most design/analysis methods assume the blades to be rigid, and thus allow the hydrodynamic pressures and structural responses to be computed separately. Moreover, most structural models only consider the mean blade load. Hence, large safety factors are often required to ensure adequate strength, stiffness, and durability. For conventional propellers, traditional methods usually lead to satisfactory design. However, blade strength and vibration considerations become increasingly important due to the use of more extreme geometries such as highly skewed propellers or supercavitating propellers. In such cases, stress concentrations, severe blade distortions, and/or resonant blade vibration may occur. Thus, a reliable method of predicting the hydrodynamic and hydroelastic blade performance is needed.

Recently, there has also been an increased interest toward flexible composite propulsors in both the marine and submarine industry. In addition to the obvious advantages of low mass and high specific strength, composite materials are more resilient to corrosion and cavitation damage. Composite materials tend to reduce life-cycle cost, allow weight

---

*Tel.: +1 609 258 5426; fax: +1 609 258 1563.
E-mail address: yyoung@princeton.edu.

0889-9746/$ - see front matter © 2006 Elsevier Ltd. All rights reserved.
doi:10.1016/j.jfluidstructs.2006.09.003

conservation, and yield better hydrodynamic and fatigue performance. Most importantly, the efficiency of the propeller can be improved via hydroelastic tailoring by exploiting the anisotropic properties of composite materials. However, these advantages can be realized only with the help of reliable methods that can accurately predict the performance of flexible propulsors in time-dependent flows.

The objective of this work is to develop a simulation tool to predict the hydroelastic performance of flexible marine propellers in nonuniform wake. The effects of fluid–structure interaction on the cavitation pattern, propeller performance, and stress distribution are investigated. To limit the scope, the current work focuses on metallic propellers with small elastic deformations. However, extension of the current method to model flexible composite material behavior is underway.

1.1. Previous work

To determine the hydrodynamic response of the propeller, vortex–lattice methods (VLMs, or lifting surface methods) and boundary element methods (BEMs, or panel methods) can be applied. The VLM was first introduced for the analysis of flow around marine propulsors by Kerwin and Lee (1978). Vortex and source lattices were placed on the mean camber surface of the blade and a robust arrangement of singularities and control points were employed to produce accurate results (Kinnas and Fine, 1989). The BEM was first applied for the analysis of marine propulsors by Hess and Valarezo (1985) using a velocity based approach, and later by Lee (1987a) using a potential based approach. Contrary to VLMs, BEMs discretized the blade surface instead of the mean camber surface, which inherently accounts for the effect of nonlinear thickness-loading coupling. Thus, BEMs offer more accurate prediction of the flow details, but require more CPU time and memory than VLMs. Although both VLMs and BEMs are potential based methods, they continue to be very efficient and reliable tools in the prediction of the hydrodynamic performance of propulsors compared to viscous solvers. However, both VLMs and BEMs assume the blades to be perfectly rigid, thus the dynamic interactions between blade deformation and fluctuating fluid pressures cannot be captured.

Since most past methods assumed the blades to be perfectly rigid, the structural response can be computed separately by applying the blade pressure obtained from the hydrodynamic model. The most extensively used structural model is based on the modified cantilever beam theory developed by Taylor (1933). It assumed the blade to be a cantilever beam loaded by thrust and torque distributed linearly over the radius (Schoenherr, 1963). Later, modifications were made to include the effects of rake, skew, and centrifugal force (Morgan, 1954; Schoenherr, 1963; Atkinson, 1968). The beam theory has been shown to be suitable for estimating the stress near the roots of propeller blade with conventional geometry and relatively narrow plan form. However, it cannot accurately predict stress distribution for complex blade geometries (e.g. propellers with high skew, wide blade outline, or vastly asymmetrical blade sections). To improve blade stress predictions, a thin-shell approach was introduced by Conolly (1961). However, due to the assumption of symmetrical forms and normal deflections, this approach was appropriate only for wide blade geometries. To overcome the limitations of shell theory, finite element methods (FEMs) have been employed for blade strength analysis since the early 1970's. Notable studies in this area include the works of Genalis (1970) using triangular plane elements, Sontvedt (1974) using thin-shell elements, Atkinson (1973) using super-parametric thick shell elements, and Ma (1974) using 3-D quadratic isoparametric brick elements. In all of these models, the fluid pressure acting on the blade surface was obtained by employing either the quasi-steady method, lifting line method, or lifting surface method. The effects of fluid–structure interactions were ignored, i.e. the fluid pressure was determined using the undeformed blade geometry. The results indicated that the FEM is more accurate than the other methods for predicting steady and unsteady blade stresses, particularly for extreme propeller geometries.

To account for change in fluid pressure due to blade deformation, an iterative procedure was developed by Atkinson and Glover (1988). A lifting surface method was used to determine the fluid pressure, which was imposed on the blade surface to obtain the change in blade geometry via a FEM, and the process was repeated until a stable operating condition was reached. The effect of cavitation was considered, but the study was limited to steady flow conditions (Atkinson and Glover, 1988). Thus, the dynamic blade stress and the effect of fluid–structure interaction on the hydrodynamic performance cannot be captured. Later, a coupled approach was introduced by Kuo and Vorus (1985) for dynamic blade stress analysis. A potential-based method was used to determine the hydrodynamic blade load, as well as the added mass and damping associated with elastic blade motion due to unsteady pressure loading. The coupled problem was solved in the frequency domain using a FEM with 3-D linear isoparametric brick elements (Kuo and Vorus, 1985). Nevertheless, the method was limited to the dynamic analysis of noncavitating fully submerged propellers, and the effect of blade displacement on the fluid pressure was ignored (i.e. the change in influence coefficients due to blade deformation were assumed to be negligible). A nonlinear coupled strategy for hydroelastic blade analysis using the FEM and lifting surface methods was also developed by Lin and Lin (1996). The change in influence coefficients due to blade displacement were included, and the effect of geometric nonlinearity was considered. However, the work was limited to steady, noncavitating propellers. Thus, the dynamic blade loads and stress distributions cannot be obtained.

Recently, Dyson (2000) and Dyson et al. (2000) presented a numerical model for the hydroelastic analysis of surface-piercing propellers. In their work, a 3-D FEM was used to model the structure. A combination of 2-D semi-loof shell elements and 3-D brick elements were used. The added mass effect of the surrounding water was included by distributing point masses across the surface of the blade according to a profile based potential flow theory around a flat plate. The total damping ratio was taken to be 0.05. To simplify the analysis, an *assumed* instead of evaluated hydrodynamic load model was applied. However, due to the over simplification of the hydrodynamic and added mass models, the method cannot provide an accurate description of the fluid–structure interaction and resulting dynamic response.

1.2. Objective of the present work

The objective of this work is to develop a simulation tool to predict the *time-dependent hydroelastic* performance of *cavitating* propellers subject to spatially varying inflow.

2. Formulation

A low-order potential-based 3-D BEM, PROPCAV, is applied to determine the moving cavity boundaries and fluctuating pressures. PROPCAV was first developed for the analysis of fully wetted marine propellers in steady flow by Lee (1987b) and Kerwin et al. (1987) and in unsteady flow by Hsin (1990) and Kinnas and Hsin (1992). The method was later extended to model the flow around 2-D partially cavitating and supercavitating hydrofoils (Kinnas and Fine, 1991), 3-D partially cavitating hydrofoils (Fine and Kinnas, 1993), and 3-D cavitating propellers (Kinnas and Fine, 1992). In Mueller and Kinnas (1999), an iterative cavity detachment search algorithm based on the Villat–Brillouin condition (Brillouin, 1911; Villat, 1914) was added to model midchord cavitation. Recently, the method has been further extended to predict simultaneous face and back cavitation on conventional fully submerged propellers (Young and Kinnas, 2001a), supercavitating propellers (Young and Kinnas, 2001b, 2003c), and surface-piercing propellers (Young and Kinnas, 2001b, 2004, 2003b; Kinnas and Young, 2003).

The commercial FEM software, ABAQUS (2004), is applied to determine the dynamic blade response. User-defined subroutines are developed to couple the BEM and FEM to include the effects of fluid–structure interaction. An overview of the formulation and implementation is provided below.

2.1. Definition of the flow field

Consider a flexible cavitating propeller subjected to a general effective inflow wake $\vec{q}_E$,[1] as shown in Fig. 1. The propeller is taken as right-handed and is assumed to be advancing with a constant forward velocity V_a. The effective inflow velocity, $\vec{q}_E$, is defined with respect to the ship-fixed coordinate system (x_s, y_s, z_s) with the origin located at the center of the hub. The x_s-axis is co-linear with the propeller axis of rotation and is positive in the downstream direction. The y_s-axis is the vertical coordinate defined positive in the direction opposite to gravity.

The propeller is assumed to be rotating at a constant angular velocity ω. To avoid the need for a moving mesh, the fluid problem is solved using a rotating blade-fixed coordinate system (x, y, z), which is attached to the reference blade. As shown in Fig. 1, the x-axis is the same as the x_s-axis, and the y-axis is co-linear with the pitch change axis with the positive direction pointing toward the blade tip. The inflow velocity, with respect to the blade-fixed coordinate system, can be expressed as follows:

$$\vec{q}_{\text{in}}(\vec{x}, t) = \vec{q}_E(x_s, r_s, \theta_s) - \vec{\Omega} \times \vec{x}, \tag{1}$$

where $r_s = \sqrt{y_s^2 + z_s^2} = \sqrt{y^2 + z^2}$, $\theta_s = \arctan(z_s/y_s) = \theta - \omega t$, $\theta = \arctan(z/y)$, and $\vec{\Omega} = [-\omega, 0, 0]^{\mathrm{T}}$.

From here on, the notation $(\vec{x}, t)$ will be dropped for simplicity since both the fluid and solid problems are solved with respect to the blade-fixed coordinate system.

---

[1] $\vec{q}_E$ is assumed to be the *effective wake*, i.e. it includes the interaction between the vorticity in the inflow and the propeller (Kinnas et al., 2000; Choi, 2000).

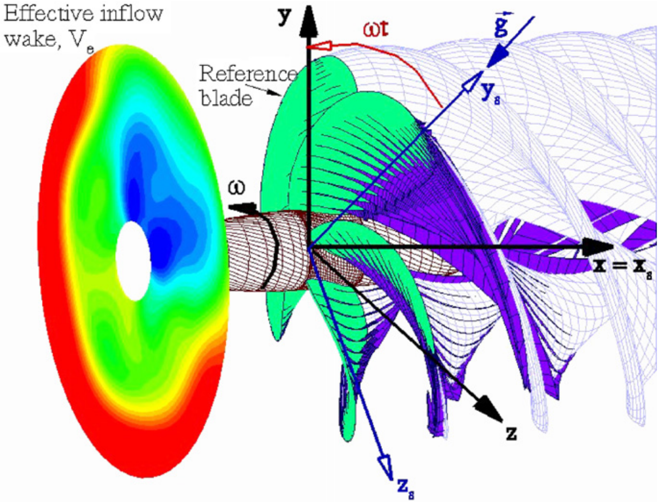

Fig. 1. Propeller subjected to a general inflow wake. The propeller-fixed coordinate system which rotates with the propeller (x, y, z) and the ship-fixed (inertial) coordinate system (x_s, y_s, z_s) are shown.

The resulting flow is assumed to be incompressible and inviscid. The total velocity, $\vec{v}$, is expressed in terms of $\vec{q}_{\text{in}}$ and the perturbation potential Φ:

$$\vec{v} = \vec{q}_{\text{in}} + \vec{\nabla}\Phi, \tag{2}$$

where Φ is the perturbation velocity potential corresponding to the propeller-induced flow field, which is assumed to be incompressible, inviscid, and irrotational.

The momentum equation with respect to the rotating blade-fixed coordinate system can be expressed as follows:

$$\frac{\partial \vec{v}}{\partial t} + (\vec{v}\cdot\vec{\nabla})\vec{v} = -\vec{\nabla}\left(\frac{P_t}{\rho}\right) + \vec{g} - \vec{\Omega}\times(\vec{\Omega}\times\vec{x}) - 2\vec{\Omega}\times\vec{v}, \tag{3}$$

where the last two terms in Eq. (3) denote the centrifugal acceleration and Coriolis acceleration, respectively; P_t is the total pressure; ρ and g are the fluid density and amplitude of the gravitational acceleration, respectively.

By applying the continuity equation $(\vec{\nabla}\cdot\vec{v} = 0)$ and making use of Eqs. (1) and (2), it can be shown that Eq. (3) can be rewritten as follows:

$$\frac{\partial \vec{q}_E}{\partial t} - \vec{v}\times(\vec{\nabla}\times\vec{q}_E) = -\vec{\nabla}H, \tag{4}$$

where $H = \partial\Phi/\partial t + P_t/\rho + \frac{1}{2}\,|\vec{v}|^2 - \vec{g}\cdot\vec{x} - \frac{1}{2}\,(\vec{\Omega}\times\vec{x})^2$.

For the case of a steady effective wake, $\partial\vec{q}_E/\partial t = 0$, integration of Eq. (4) between two points on the same streamline yields H = constant along the streamline. Applying Eq. (1), the absolute total pressure P_t can be computed as follows:

$$P_t = P_o + \rho\left[\frac{1}{2}|\vec{q}_{\text{in}}|^2 - \frac{\partial\Phi}{\partial t} - \frac{1}{2}|\vec{v}|^2\right], \tag{5}$$

where $P_o = P_{\text{atm}} + \rho g d_s$ is the absolute hydrostatic pressure at $\vec{x}$; P_{atm} is the atmospheric pressure and d_s is the submerged depth of point $\vec{x}$ from the free surface.

2.2. *Governing equation for the fluid*

The fluid problem is solved with respect to perturbation potential Φ in the blade-fixed coordinate system (x, y, z), which is governed by the Laplace equation, $\nabla^2\Phi = 0$.

For small blade deformations, Φ, can be linearly decomposed into two parts:

$$\Phi = \phi + \varphi, \tag{6}$$

where ϕ denotes the perturbation potential due to rigid blades rotating in a nonuniform wake, and φ denotes the perturbation potential due to the vibrating blades in uniform wake.

Thus, the total velocity (Eq. (2)) can be rewritten as

$$\vec{v} = \vec{q}_{\text{in}} + \vec{\nabla}\phi + \vec{\nabla}\varphi = \vec{q} + \vec{\nabla}\varphi, \tag{7}$$

where $\vec{q} = \vec{q}_{\text{in}} + \vec{\nabla}\phi$ is the fluid velocity due to rigid blades rotating in nonuniform wake; $\vec{\nabla}\varphi$ is the fluid velocity due to vibrating blades in uniform wake.

Similarly, the total pressure, $P_t = P + P_v$, can also be decomposed into a part due to rigid blade motion, P, and a part due to elastic blade deformation, P_v:

$$P = P_o + \rho\left[\frac{1}{2}|\vec{q}_{\text{in}}|^2 - \frac{\partial\phi}{\partial t} - \frac{1}{2}|\vec{q}|^2\right], \tag{8}$$

$$P_v = \rho\left[-\frac{\partial\varphi}{\partial t} - \vec{q}_{\text{in}}\cdot\vec{\nabla}\varphi\right], \tag{9}$$

using the relations $\partial\Phi/\partial t = \partial\phi/\partial t + \partial\varphi/\partial t$ and $|\vec{v}|^2 = |\vec{q}|^2 + 2\vec{q}\cdot\vec{\nabla}\varphi + |\vec{\nabla}\varphi|^2 \approx |\vec{q}|^2 + 2\vec{q}_{\text{in}}\cdot\vec{\nabla}\varphi$.

2.3. Governing equation for the solid

The dynamic equation of motion with respect to the blade-fixed coordinate system can be written as follows:

$$[M]\{\ddot{u}\} + [D]\{\dot{u}\} + [K]\{u\} = \{F_c\} + \{F\} + \{f\}, \tag{10}$$

where $\{\ddot{u}\}$, $\{\dot{u}\}$, and $\{u\}$ are the nodal acceleration, velocity, and displacement vectors, respectively. $[M] = \int \rho_s[N]^{\mathrm{T}}[N]\,\mathrm{d}V$, $[D] = \int \mathrm{d}[N]^{\mathrm{T}}[N]\,\mathrm{d}V$, and $[K] = \int[B]^{\mathrm{T}}[E][B]$ are the structural mass matrix, damping matrix, and stiffness matrix, respectively. $[N]$, $[B] = [\partial][N]$, and $[E]$ are the displacement interpolation matrix, strain-displacement matrix, and material constitutive matrix, respectively; ρ_s and d are the mass density and viscous damping, respectively, of the blade. In the current model, the blades are assumed to be made of a homogeneous, isotropic, and linear elastic material. Thus, the material properties can be represented by Young's modulus E and Poisson's ratio v.

2.4. Inertial and hydrodynamic forces

The nodal force vectors on the right-hand side of Eq. (10) represent the centrifugal force ($\{F_c\}$), hydrodynamic force due to with rigid blade rotating in nonuniform wake ($\{F\}$), and hyrodynamic force due to elastic blade deformation ($\{f\}$), respectively. The centrifugal force ($\vec{F}_c = -m\vec{\Omega} \times [\vec{\Omega} \times (\vec{x} + \vec{u})]$) contributes to the load stiffness matrix, and is applied as element based loads in ABAQUS (2004). It should be noted that the Coriolis force, which contributes to the load damping matrix, is assumed to be negligible due to the small deformations. The hydrodynamic force vectors, $\{F\}$ and $\{f\}$, are computed by integrating the corresponding pressures over the blade surface:

$$\{F\} = \int [N]^{\mathrm{T}}\{P\}\,\mathrm{d}S, \quad \{f\} = \int [N]^{\mathrm{T}}\{P_v\}\,\mathrm{d}S. \tag{11,12}$$

To solve Eq. (10), the values of perturbation velocity potentials (ϕ and φ) are needed to determine the fluctuating fluid pressures (P as given by Eq. (8) and P_v as given by Eq. (9)). In this work, the fluid problem is linearly decomposed into two parts: rigid blades rotating in nonuniform wake and flexible blades vibrating in uniform wake. Thus, ϕ is obtained by solving the rigid blade problem, and φ is obtained by solving the vibrating blade problem. Both ϕ and φ are governed by the Laplace equation, and thus can be reduced to a boundary value problem over the blade, hub, cavity, and wake surfaces, which can be solved using a 3-D potential-based BEM. The velocity compatibility and pressure equilibrium conditions are imposed on the blade surface, which provides the kinematic boundary condition for the fluid model and the surface traction for the solid model, respectively. The fluid–structure interaction algorithm is similar to that presented in Kuo and Vorus (1985), but the problem is solved in the time domain and the effect of hydrodynamic cavitation is considered.

In the sections that follow, the formulation and implementation of the two parts of the fluid problem are presented, followed by a detailed explanation of the coupling procedure between the BEM and FEM to capture the fluid–structure interactions.

2.5. Hydrodynamic analysis of the rigid blade problem

The perturbation potential due to rigid blades rotating in nonuniform wake, ϕ, at every point p on the combined wetted blade and cavity surface, $S_{WB}(t) \cup S_C(t)$, is given by Green's third identity:

$$\begin{aligned} 2\pi\phi_p(t) = & \int\int_{S_{WB}(t)\cup S_C(t)} \left[\phi_q(t)\frac{\partial G(p;q)}{\partial n_q(t)} - G(p;q)\frac{\partial \phi_q(t)}{\partial n_q(t)}\right] \mathrm{d}S \\ & + \int\int_{S_W} \Delta\phi(r_q,\theta_q,t)\frac{\partial G(p;q)}{\partial n_q(t)}\,\mathrm{d}S; \quad p \in S_{WB}(t)\cup S_C(t), \end{aligned} \tag{13}$$

where the subscript q corresponds to the variable point in the integration. $G(p;q) = 1/R(p;q)$ is Green's function in an unbounded 3-D fluid domain, with $R(p;q)$ being the distance between points p and q; $\vec{n}_q$ is the unit vector normal to the integration surface, with the positive direction pointing into the fluid domain. $S_{WB}(t)$ denotes the wetted blade and hub surfaces, and $S_C(t)$ denotes the cavitating/ventilated surfaces.

The wake surface, S_W, is assumed to have zero thickness and its geometry is determined by satisfying the *force-free* condition. The iterative lifting surface method developed by Greeley and Kerwin (1982) is used to align the wake with the circumferentially averaged inflow. The dipole strength $\Delta\phi(r,\theta,t)$ on the wake surface is determined as follows:

$$\Delta\phi(r,\theta,t) = \Delta\phi\left(r_T, t - \frac{\theta-\theta_T}{\omega}\right), \tag{14}$$

where (r,θ) are the cylindrical coordinates at any point in the trailing wake surface, and (r_T,θ_T) are the blade trailing edge coordinates of the corresponding streamline.

The value of the dipole strength, $\Delta\phi(r_T,t)$, at the trailing edge of the blade at radius r_T and time t, is given by Morino's Kutta condition (Morino and Kuo, 1974):

$$\Delta\phi(r_T,t) = \phi^+(r_T,t) - \phi^-(r_T,t), \tag{15}$$

where $\phi^+(r_T,t)$ and $\phi^-(r_T,t)$ are the values of the ϕ at the upper (suction side) and the lower (pressure side) blade trailing edge, respectively, at time t.

2.5.1. Kinematic boundary condition on wetted blade and hub surfaces

The kinematic boundary condition requires the flow to be tangent to the wetted blade and hub surface, which forms a Neumann-type boundary condition:

$$\frac{\partial\phi}{\partial n} = -\vec{q}_{\mathrm{in}}\cdot\vec{n}. \tag{16}$$

2.5.2. Dynamic boundary condition on cavitating surfaces

The dynamic boundary condition on the cavitating blade and wake surfaces requires the pressure everywhere on the cavity to be constant and equal to the prescribed cavity pressure: $P = P_c$. For fully submerged propellers, P_c is equal to the saturated vapor pressure of the liquid; for partially submerged or ventilated propellers, P_c is equal to the atmospheric pressure.

By applying Bernoulli's equation, the total cavity velocity, $\vec{q}_c$, can be expressed as follows:

$$|\vec{q}_c|^2 = n^2D^2\sigma_n + |\vec{q}_{\mathrm{in}}|^2 - 2\frac{\partial\phi}{\partial t}, \tag{17}$$

where $\sigma_n \equiv (P_o - P_c)/(\frac{1}{2}\rho n^2 D^2)$ is the cavitation number; $n = \omega/2\pi$ and D are the propeller rotational frequency and diameter, respectively. It can be shown that Eq. (17) can be converted to a Dirichlet-type boundary condition for ϕ (Fine, 1992).

2.5.3. Kinematic boundary condition on cavitating surfaces

The height of the cavity (h), defined normal to the blade surface, is given by the kinematic boundary condition, which requires that the total velocity normal to the cavity surface to be zero:

$$\frac{D}{Dt}(n - h(s,v,t)) = \left[\frac{\partial}{\partial t} + \vec{q}_c(x,y,z,t)\cdot\vec{\nabla}\right](n - h(s,v,t)) = 0, \tag{18}$$

where s, v, and n are the local curvilinear coordinates as shown in Fig. 2.

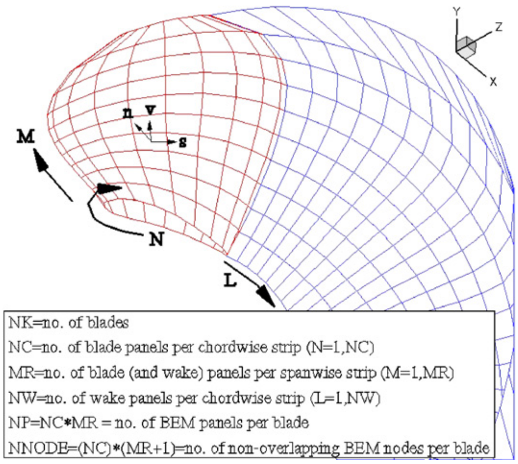

Fig. 2. BEM discretization of the blade and wake surfaces.

2.5.4. *Cavity closure condition*

The height and extent of the moving cavity boundary are unknown and have to be determined as part of the solution. The cavity length at each radius r and time t is given by the function $l(r,t)$. For a given cavitation number, σ_n, the cavity planform, $l(r,t)$, must satisfy the following condition:

$$\delta_c(l(r,t); r, \sigma_n) = 0, \tag{19}$$

where δ_c is the thickness of the cavity trailing edge. Eq. (19) requires that the cavity closes at its trailing edge.

2.5.5. *Numerical algorithm*

The integral surfaces are approximated with hyperboloidal panels (Kinnas and Hsin, 1992) on which constant strength dipoles and sources are distributed. An example of the discretized blade and wake surface is shown in Fig. 2. A constant time increment, Δt, is used. At each time step, the propeller blades rotate by a blade angle increment $\Delta\theta = \omega\Delta t$, and the solution is only obtained for the key (i.e. reference) blade. The influence of the other blades is accounted for in a progressive manner by using the solution from an earlier time step when the key blade was in the position of that blade. A second-order moving least-squares derivative recovery method (Tabbara et al., 1994) is used to compute the time derivatives.

The discretized form of Eq. (13) can be written as follows:

$$2\pi\phi_i = \sum_{k=1}^{NK}\sum_{m=1}^{MR}\left\{\sum_{n=1}^{NC}\left[A'_{i,m,n,k}\phi_{m,n,k}(t) - B'_{i,m,n,k}\frac{\partial\phi}{\partial n_{m,n,k}}(t)\right] + \sum_{l=1}^{NW}\left[W_{i,m,l,k}\Delta\phi_{m,l,k}(t) - G_{i,m,l,k}Q_{m,l,k}(t)\right]\right\}$$
$$\text{for } i = 1,\ldots, MR \times (NC + NCW(m,t)), \tag{20}$$

where $A'_{i,m,n,k}$ represent the potential induced at the ith control point on the key blade by an unit strength dipole at the nth panel on the mth strip of the kth blade. Note that $k=1$ refers to the key blade. Similarly, $B'_{i,m,n,k}$, $G_{i,m,l,k}$, and $W_{i,m,l,k}$ represent the influence coefficients due to unit strength source on the blade, unit strength source on the cavitating portion of the wake, and unit strength dipole on the wake, respectively. $Q_{m,l,k}$ and $\Delta\phi_{m,l,k}$ represent the cavity source strength and potential jump, respectively, on the lth panel of the mth strip of the kth blade wake. The quantities NK, MR, NC, NW are defined in Fig. 2. $NCW(m,k,t)$ is the number of cavitating wake panels on the mth strip of the kth blade at time t.

Eq. (20) can be more generally expressed in matrix form as

$$[A]\{\phi\} = [B]\left\{\frac{\partial\phi}{\partial n}\right\}, \tag{21}$$

where $[A]$ and $[B]$ denote the dipole and source, respectively, influence coefficient matrices.

The known values of ϕ and $\partial\phi/\partial n$ are given by boundary conditions specified in Eqs. (14)–(17). The cavity heights on the blade and the wake are computed by applying the flow tangency condition on the cavitating surfaces (Eq. (18)). The correct cavity planform at each time step is obtained iteratively using a Newton–Raphson technique until the cavity closure condition (Eq. (19)) is satisfied. A *split* panel technique (Kinnas and Fine, 1993; Fine, 1992) is used to treat panels intersected by the cavity trailing edge. The cavity detachment location is determined in an iterative manner by applying the Villat–Brillouin smooth detachment condition (Brillouin, 1911; Villat, 1914). Once the values of ϕ are known on all the blade panels at each time step, the hydrodynamic pressure, P, is given by Eq. (8). Finally, the hydrodynamic force for the rigid blade problem, F, in Eq. (10), can be obtained by integrating the P over the blade surface (i.e. Eq. (11)).

Details of the numerical implementation of the BEM for the rigid blade problem and extensive numerical and experimental validation studies are given in Young and Kinnas (2001a, 2003c), Kinnas and Young (2003) and Kinnas et al. (2003a).

2.6. Hydrodynamic analysis of the vibrating blade problem

The perturbation potential due to flexible blades vibrating in uniform wake, φ, at every point p can also be determined using Green's third identity:

$$2\pi\varphi_p(t) = \int\int_{S_B}\left[\varphi_q(t)\frac{\partial G(p;q)}{\partial n_q(t)} - G(p;q)\frac{\partial \varphi_q(t)}{\partial n_q(t)}\right]\mathrm{d}S + \int\int_{S_W}\Delta\varphi(r_q,\theta_q,t)\frac{\partial G(p;q)}{\partial n_q(t)}\,\mathrm{d}S; \quad p \in S_B, \tag{22}$$

where S_B denote the blade and hub surfaces. Eq. (22) can be rewritten in matrix form as

$$[A]\{\varphi\} = [B]\left\{\frac{\partial\varphi}{\partial n}\right\}, \tag{23}$$

where the influence coefficient matrices $[A]$ and $[B]$ are the same as those for the rigid blade BEM analysis (Eq. (21)). The implicit assumption is that the change in influence coefficients with time is negligible, which is valid for small blade deformations.

Multiplying both sides of Eq. (23) by $[A]^{-1}$ yields the following expression for φ:

$$\{\varphi\} = [C]\left\{\frac{\partial\varphi}{\partial n}\right\}, \tag{24}$$

where $[C] = [A]^{-1}[B]$.

Similarly, the i-component of the spatial derivative of φ can be computed as follows:

$$\begin{aligned}2\pi\frac{\partial\varphi_p}{\partial x_i}(t) = {} & \int\int_{S_B}\left[\varphi_q(t)\frac{\partial}{\partial x_i}\frac{\partial G(p;q)}{\partial n_q(t)} - \frac{\partial G(p;q)}{\partial x_i}\frac{\partial\varphi_q(t)}{\partial n_q(t)}\right]\mathrm{d}S \\ & + \int\int_{S_W}\Delta\varphi(r_q,\theta_q,t)\frac{\partial}{\partial x_i}\frac{\partial G(p;q)}{\partial n_q(t)}\,\mathrm{d}S; \quad p \in S_B,\end{aligned} \tag{25}$$

which can be expressed in matrix form as

$$\left\{\frac{\partial\varphi}{\partial x_i}\right\} = [A_{x_i}]\{\varphi\} - [B_{x_i}]\left\{\frac{\partial\varphi}{\partial n}\right\}, \tag{26}$$

where $[A_{x_i}]$ and $[B_{x_i}]$ are the coefficient matrices representing the i-component of the induced velocities due to unit strength dipoles and sources, respectively.

Applying Eqs. (24) and (26) can be rewritten as follows:

$$\left\{\frac{\partial\varphi}{\partial x_i}\right\} = [A_{x_i}][C]\left\{\frac{\partial\varphi}{\partial n}\right\} - [B_{x_i}]\left\{\frac{\partial\varphi}{\partial n}\right\} = [C_{x_i}]\left\{\frac{\partial\varphi}{\partial n}\right\}, \tag{27}$$

where $[C_{x_i}] = [A_{x_i}][C] - [B_{x_i}]$.

2.6.1. Kinematic boundary condition on blade surface

The velocity compatibility condition requires the normal components of the fluid velocity and solid body velocity to be equal at the blade surface. Applying linear decomposition, it can be shown that the no penetration conditions reduces to (Vorus, 1981; Kuo, 1984; Young and Kinnas, 2003b):

$$\frac{\partial\phi}{\partial n} = -\vec{q}_{\mathrm{in}}\cdot\vec{n} \tag{28}$$

$$\frac{\partial\varphi}{\partial n} = \frac{\partial\vec{\delta}}{\partial t}\cdot\vec{n} + [(\nabla\phi\cdot\nabla)\vec{\delta} - (\vec{\delta}\cdot\nabla)(\nabla\phi)]\cdot\vec{n} \approx \frac{\partial\vec{\delta}}{\partial t}\cdot\vec{n}, \tag{29}$$

where Eq. (28) is the kinematic boundary condition for the rigid blade case (same as Eq. (16)), and Eq. (29) is the kinematic boundary condition for the elastic blade case. $\vec{\delta}$ is the displacement vector at the element centroid, and is a function of the material coordinates of the blade in the rotating blade-fixed coordinates system.

Defining $[T]$ as the transformation matrix which relates the normal velocities at the element centroids to the element nodal velocities (i.e. $(\partial\vec{\delta}/\partial t)\cdot\vec{n} = [T]\{\dot{u}\}$), Eq. (29) can be rewritten as follows:

$$\frac{\partial\varphi}{\partial n} = [T]\{\dot{u}\}. \tag{30}$$

2.6.2. Time-dependent hydroelastic pressure

The hydroelastic pressure, P_v, can be computed by applying Eq. (9). The values of $\{\varphi\}$ and $\{\partial\varphi/\partial x_i\}$ can be obtained by applying Eq. (30) to Eqs. (24) and (27):

$$\{\varphi\} = [C][T]\{\dot{u}\}, \quad \left\{\frac{\partial\varphi}{\partial x_i}\right\} = [C_{x_i}][T]\{\dot{u}\}. \tag{31,32}$$

In this work, the influence coefficients are assumed to be independent of time. Thus, the partial time derivative of φ can be computed as follows:

$$\left\{\frac{\partial\varphi}{\partial t}\right\} = [C][T]\{\ddot{u}\}. \tag{33}$$

Hence, the hydroelastic pressure defined in Eq. (9) can be rewritten as follows:

$$\{P_v\} = -\rho[C][T]\{\ddot{u}\} - \rho[QC][T]\{\dot{u}\},$$

where $[QC] = \{q_{\text{in}_1}\}^{\text{T}}[C_{x_1}] + \{q_{\text{in}_2}\}^{\text{T}}[C_{x_2}] + \{q_{\text{in}_3}\}^{\text{T}}[C_{x_3}]$ and $(q_{\text{in}_1}, q_{\text{in}_2}, q_{\text{in}_3})$ are the three components of the inflow velocity vector, $\vec{q}_{\text{in}}$.

2.7. Fluid–structure interaction

In order to obtain the vibratory perturbation potential φ and hydroelastic pressure P_v via BEM analysis, the solid body velocities ($\dot{u}$) and accelerations ($\ddot{u}$) are needed from the FEM analysis. In turn, the FEM analysis requires the hydrodynamic pressures (P and P_v) from the BEM analysis to solve for the dynamic blade motions (u, $\dot{u}$, and $\ddot{u}$). In this work, the fluid structure interaction problem is solved by expressing the blade motion dependent hydroelastic force ($\{f\} = \int [N]^{\text{T}}\{P_v\}\,\text{d}S$, Eq. (12)) in terms of added mass ($[M^h]$) and hydrodynamic damping ($[D^h]$), and placing the terms in the left-hand side of the equilibrium equation of motion, Eq. (10):

$$([M] + [M^h])\{\ddot{u}(t)\} + ([D] + [D^h])\{\dot{u}(t)\} + [K]\{u(t)\} = \{F(t)\} + \{F_c\}, \tag{34}$$

where

$$[M^h] = \rho\int [N]^{\text{T}}[C][T]\,\text{d}S, \quad [D^h] = \rho\int [N]^{\text{T}}[QC][T]\,\text{d}S. \tag{35,36}$$

2.7.1. Added-mass matrix

To compute the added-mass matrix, $[M^h]$, the transformation matrix, $[T]$, is needed to relate the normal velocities at the centroid of the BEM elements to the nodal velocities of the FEM elements. Representing the normal velocity at the centroid of the jth BEM panel as the average of the normal velocities at the four corner nodes (see Fig. 3), Eq. (30) can be rewritten as follows:

$$\frac{\partial\varphi}{\partial n_j} = [T_j]\{\dot{U}_j\}, \tag{37}$$

where

$$[T_j] = \tfrac{1}{4}[n_x^j \; n_y^j \; n_z^j \; n_x^j \; n_y^j \; n_z^j \; n_x^j \; n_y^j \; n_z^j \; n_x^j \; n_y^j \; n_z^j],$$
$$\{\dot{U}_j\} = [\dot{U}_{j1} \; \dot{V}_{j1} \; \dot{W}_{j1} \; \dot{U}_{j2} \; \dot{V}_{j2} \; \dot{W}_{j2} \; \dot{U}_{j3} \; \dot{V}_{j3} \; \dot{W}_{j3} \; \dot{U}_{j4} \; \dot{V}_{j4} \; \dot{W}_{j4}]^{\text{T}};$$

$\dot{U}_{jl}$, $\dot{V}_{jl}$, $\dot{W}_{jl}$ are the x, y, and z components, respectively, of the velocity vector at the lth corner node of panel j; $\{\vec{n}_j\} = [n_x^j \; n_y^j \; n_z^j]^{\text{T}}$ is the unit normal vector at the centroid of the jth panel, pointing into the fluid domain.

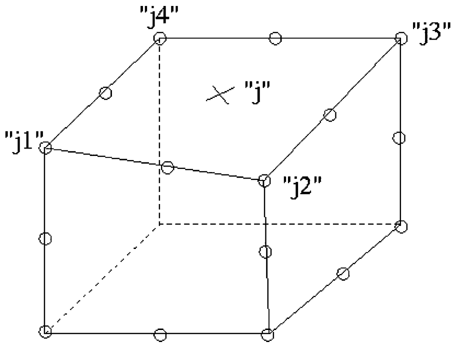

Fig. 3. The centroid and four corner nodes of the jth BEM element.

Applying Eq. (37), Eq. (31) can be rewritten as follows:

$$\varphi_i = \sum_{j=1}^{NP} C_{ij}[T_j]\{\dot{U}_j\}, \tag{38}$$

where $NP = MR \times NC$ is the number of BEM panels per blade, as shown in Fig. 2.

The hydroelastic pressure associated with fluid acceleration at panel i can be calculated as

$$(P_v)_i = -\rho \frac{\partial \varphi}{\partial t}_i = -\rho \sum_{j=1}^{NP} C_{ij}[T_j]\{\ddot{U}_j\}. \tag{39}$$

Distributing the force vector associated with fluid acceleration equally among the four corner nodes on panel i, the elemental added-mass matrix, $[M^h_{ij}]$, given by Eq. (35), can be written as follows:

$$[M^h_{ij}] = \rho S_i C_{ij}[T_i]^{\mathrm{T}}[T_j], \tag{40}$$

where S_i is the surface area of panel i.

Assembling the three degrees of freedom of each BEM node in x, y, z order, the global consistent added mass matrix $[M^h]$ can be written as

$$[M^h] = \begin{bmatrix} m^h_{1,1} & m^h_{1,2} & \cdots & m^h_{1,3(NNODE)} \\ m^h_{2,1} & m^h_{2,2} & \cdots & m^h_{2,3(NNODE)} \\ \vdots & \vdots & \ddots & \vdots \\ m^h_{3(NNODE),1} & m^h_{3(NNODE),2} & \cdots & m^h_{3(NNODE),3(NNODE)} \end{bmatrix}, \tag{41}$$

where $NNODE = NC \times (MR + 1)$ is the number of nonoverlapping BEM nodes per blade (see Fig. 2). Each element in the added mass matrix, $m^h_{i,j}$, represent the hydrodynamic force imposed at the ith degree of freedom due to unit nodal accelerations at the jth degree of freedom. For example, $m^h_{2,3(NNODE)}$ represent the y-component of the hydrodynamic force exerted at node 1 due to unit acceleration in the z-direction of node $NNODE$.

In general, the matrix of influence coefficients, $[C]$, is full and asymmetric. Thus, $[M^h]$ will also be full and asymmetric. To reduce computational cost and storage requirement, a HRZ-like lumping technique is applied to replace $[M^h]$ with the diagonally-lumped added-mass matrix, $[M^{Lh}]$. It is obtained by scaling diagonal entries of the consistent added-mass matrix with the ratio of the sum of the entries that contribute to the motion in the same direction over the sum of the diagonal entries that contribute to the motion in that direction:

$$[M^{Lh}] = \begin{bmatrix} m^{Lh}_1 & 0 & 0 & 0 \\ 0 & m^{Lh}_2 & 0 & 0 \\ 0 & 0 & \ddots & 0 \\ 0 & 0 & 0 & m^{Lh}_{3(NNODE)} \end{bmatrix}, \tag{42}$$

where m_i^{Lh} denotes the lumped added mass for the ith degree of freedom, and is calculated as

$$m^{Lh}_{3(i-1)+k} = m^h_{3(i-1)+k,3(i-1)+k} \frac{\sum_{l=1}^{NNODE} \sum_{j=1}^{NNODE} m^h_{3(l-1)+k,3(j-1)+k}}{\sum_{j=1}^{NNODE} m^h_{3(j-1)+k,3(j-1)+k}} \tag{43}$$

for $k = 1, 2, 3$ and $i = 1, 2, \ldots, NNODE$.

The above mass diagonalization method is simple to implement and it ensures the total added-mass for each translational degrees of freedom is conserved. The resulting lumped added-mass is decoupled for each degree of freedom, and thus can be easily superimposed to the structural mass matrix. The HRZ-like lumping technique can be interpreted as a method of distributing the total fluid inertial force in each direction to the degrees of freedom that contribute to the motion in that direction. Hence, the lumped mass idealization is sufficient to capture the net effect of fluid–structure interaction on the hydrodynamic performance and dynamic blade motion.

2.7.2. Hydrodynamic damping matrix

The hydrodynamic damping matrix is generated in a similar fashion as the added-mass matrix. It can be shown that the elemental hydrodynamic damping matrix, $[D^h_{ij}]$, given by Eq. (36), can be written as follows:

$$[D^h_{ij}] = \rho S_i (QC_{ij}) [T_i]^{\mathrm{T}} [T_j]. \tag{44}$$

Since the resulting global hydrodynamic damping matrix will also be full and asymmetric, the same lumping procedure is applied to replace $[D^h]$ with the diagonally-lumped hydrodynamic damping matrix, $[D^{Lh}]$.

2.8. Numerical algorithm

The fluid–structure interaction problem is solved by coupling the presented BEM (PROPCAV) with a commercial FEM software (ABAQUS). The BEM is applied to determine the hydrodynamic load vector due to rigid blades ($\{F(t)\}$), the lumped added-mass matrix ($[M^{Lh}]$), and the lumped hydrodynamic damping matrix ($[D^{Lh}]$), all of which are read by the FEM as inputs via user-defined subroutines. The FEM is then employed to solve the following system of equations:

$$([M] + [M^{Lh}])\{\ddot{U}(t)\} + ([D] + [D^{Lh}])\{\dot{U}(t)\} + [K]\{U(t)\} = \{F(t)\} + \{F_c\}. \tag{45}$$

The Hilber–Hughes–Taylor implicit direct integration method in ABAQUS (2004) is applied to calculate the dynamic blade response.

In the FEM model, one-layer of quadratic 3-D solid elements is used across the blade thickness. Quadratic elements are necessary to avoid hour-glass and shear-lock failures associated with first-order elements. To avoid the need for interpolation in the BEM/FEM coupling, the exterior nodes of the finite elements are set to coincide with the end-nodes of the BEM. Thus, $NC \times MR$ (chordwise×spanwise) BEM surface panels is equivalent to $NC/2 \times MR$ FEM solid volumetric elements. To allow for general blade geometry, a combination of 20-node reduced integration brick (C3D20R) elements and 15-node triangular (C3D15) elements are used to represent the blade. The nodes at the root of the blade are fixed in the structural model, i.e. the blades are assumed to be rigidly attached to the hub. The current model also assumes the blade to be made of homogeneous, isotropic, linear elastic material.

The lumped added-mass and hydrodynamic damping matrices are superimposed onto the structural added mass and damping matrices via the use of user-defined hydroelastic elements. Each hydroelastic element has only one node, and each node has three degrees of freedom. The hydroelastic elements have no stiffness; thus they only contribute to the total mass and damping of the system. The three vector components of the added-mass, $m^{Lh}_{3(i-1)+k}$, associated with the three degrees of freedom ($k = 1, 2, 3$) for each hydroelastic element is given by Eq. (43). A similar procedure is used to define the three vector components of the hydrodynamic damping, $d^{Lh}_{3(i-1)+k}$, for each hydroelastic element. A total of $NNODE$ hydroelastic elements are employed, and they are located on the FEM nodes that coincide with the BEM nodes.

The resulting hydroelastic force due to blade vibration, $\{f(t)\}$, is computed as follows:

$$\{f(t)\} = -[M^{Lh}]\{\ddot{U}(t)\} - [D^{Lh}]\{\dot{U}(t)\}. \tag{46}$$

The total hydrodynamic blade load, $\{f_{\mathrm{tot}}(t)\}$, is defined as

$$\{f_{\mathrm{tot}}(t)\} = \{F(t)\} + \{f(t)\}. \tag{47}$$

2.9. Natural frequencies and mode shapes

To avoid expensive complex eigenvalue extraction, the damping matrices are neglected in the current eigenvalue analysis. Thus, the eigenvalue problem is solved as follows:

$$(-\omega^2([M] + [M^{Lh}]) + [K])\{\Psi\} = 0, \tag{48}$$

where ω denote the circular frequencies.

3. BEM validation studies

Extensive numerical convergence and experimental validation studies of the current BEM model has been conducted and are presented in Kinnas and Fine (1992), Young and Kinnas (2001a,2003a–c,2004), and Kinnas et al. (2003b). Examples of comparisons between predicted and measured propeller blade loads and cavitation patterns in steady and unsteady conditions are shown here for the sake of completeness.

3.1. Steady performance

Examples of the predicted and measured blade forces and cavitation patterns for a 72° skew propeller (NSRDC propeller 4383) is shown in Fig. 4. The propeller geometry is given in Boswell (1971) and Cumming et al. (1972), and is shown in Fig. 4. Open water performance tests were conducted at the NSRDC deep water basin, and cavitation tests were conducted in a 0.6096 m (24 in) cavitation tunnel at NSRDC (Boswell, 1971). As shown in the figure, the numerical predictions are in good agreement with experimental measurements for a wide range of flow conditions. In addition, the predicted cavitation patterns seem reasonable.

3.2. Unsteady performance

Comparisons between the predicted versus observed unsteady cavitation patterns for a three bladed, zero-skew, zero-rake propeller (DTMB propeller 4148) is shown in Fig. 5. The propeller geometry is given in Kinnas and Pyo (1999), and is shown in Fig. 5. Also shown in the figure is the effective inflow wake, which corresponds to the screen generated nonaxisymmetric inflow inside a cavitation tunnel given in Mishima et al. (1995) with the effects of the tunnel walls and vortical inflow/propeller interactions (nonaxisymmetric "effective" wake) accounted for by using the method of

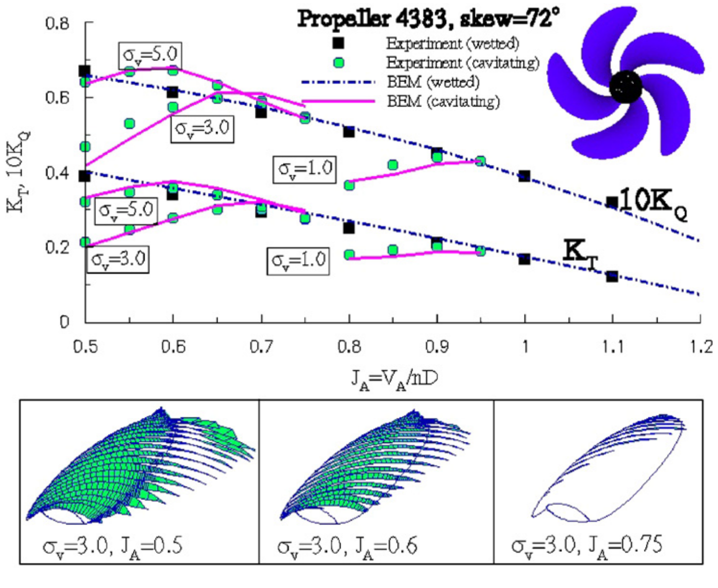

σ_v=3.0, J_A=0.5 σ_v=3.0, J_A=0.6 σ_v=3.0, J_A=0.75

Fig. 4. Predicted and measured thrust ($K_T = T/\rho n^2 D^4$) and torque ($K_Q = T/\rho n^2 D^5$) coefficients as a function of the cavitation number ($\sigma_v = \sigma_n/J_A^2 = (P_o - P_c)/(\frac{1}{2}\rho n^2 D^2 J_A^2)$) and advance ratio ($J_A = V_A/nD$) for propeller 4383. Also shown are the predicted cavitation patterns at three different J_A for $\sigma_v = 3.0$.

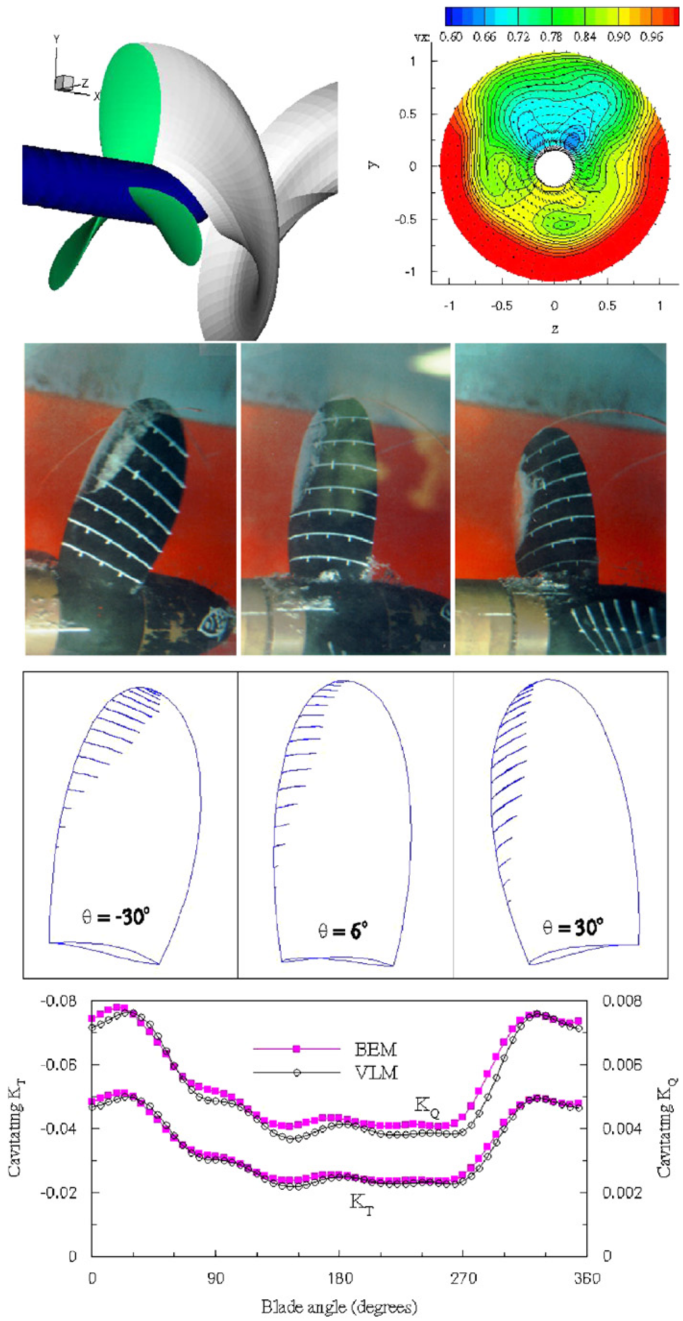

Fig. 5. Top: geometry and effective wake of propeller DTMB4148. Middle: Observed versus predicted unsteady cavitation patterns. Bottom: Comparison of the cavitating blade loads predicted by the current BEM and by a 3-D vortex lattice method (VLM).

(Kinnas et al., 2000; Choi, 2000). The flow conditions are as follows: $\sigma_n = (P_o - P_c)/(\frac{1}{2}\rho n^2 D^2) = 2.576$, $J_A = V_A/nD = 0.9087$, and $F_r = n^2 D/g = 9.159$. The equivalent J_A, 0.957, for unbounded flow is obtained by matching the fully wetted thrust (T) coefficient, $K_T = T/\rho n^2 D^4$, with the measured K_T, 0.0993, from experiment. Comparisons of the predicted cavitating thrust and torque coefficients with those produced using a 3-D VLM, MPUF-3A (Lee et al., 2001), is shown in the bottom of Fig. 5. It can be observed that the predicted cavitation patterns compared well with experimental observations, and the predicted dynamic blade loads compared well with the 3-D

VLM. The minor discrepancy between the predicted and observed cavitation patterns near the blade tip region is probably due to the formation of tip–vortex cavity which was not modelled in the current BEM.

4. FEM validation studies

4.1. Twisted cantilever plate

To assess the accuracy of the current FEM in predicting the vibrational frequencies and mode shapes of propeller blades, a systematic parametric study is conducted for a twisted cantilever plate shown in Fig. 6. The span (A) to chord (B) ratio of the plate is 3.0; the thickness (H) to chord (B) ratio is $\frac{1}{20}$; and the twist angle ϕ is 30°. This plate is one of a series of 30 nonrotating cantilever plates tested by MacBain et al. (1985) as part of a joint government/industry/university effort to assess the accuracy of state-of-the-art numerical methods in computing the natural frequencies and

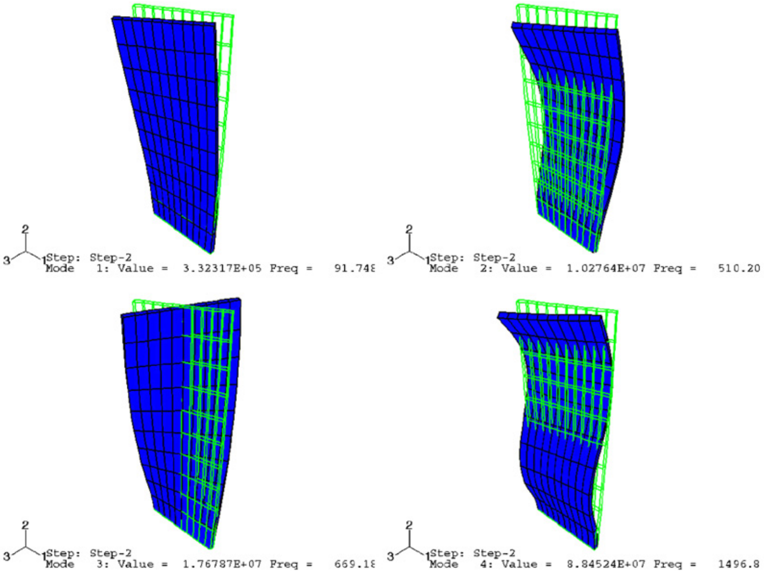

Fig. 6. Predicted mode shapes for a twisted cantilever blades. 10 × 10 × 1 C3D20R elements.

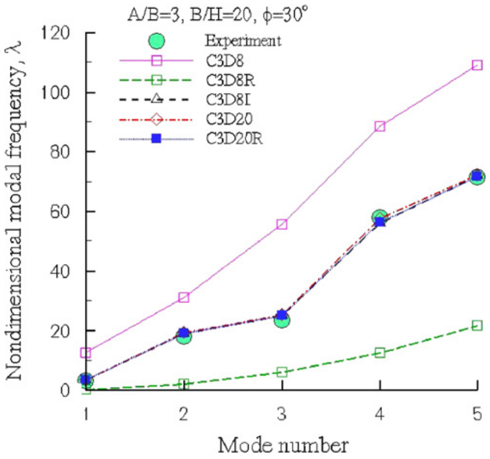

Fig. 7. Comparisons of the predicted and measured frequency parameters for different types of continuum solid elements. 10 × 10 × 1 elements.

mode shapes of turbomachinery blades. The specimens were precision-machined at the Air Force Aero Propulsion Laboratory from 7075-T6 cold drawn aluminium bar stock, and the width of all the specimens was 5.08 cm (2 in). The measured material properties are: ρ_s (solid density) $= 2795.7\,\text{kg/m}^3$, E (Young' s modulus) $= 71.3\,\text{GPa}$, v (Poisson' s ratio) $= 0.3$. The test specimens were carefully tested at two separate laboratories (MacBain et al., 1985; Kielb et al., 1985), and the maximum error in the measured frequency is 1.7% based on material property and geometric tolerances (MacBain et al., 1985). Details of experimental and theoretical investigation of the vibrational characteristics of the plates can be found in MacBain et al. (1985) and Kielb et al. (1985), respectively. Examples of the predicted mode shapes for the first four modes are shown in Fig. 6. Comparison of the predicted versus measured frequencies (in air) for different types of continuum solid elements are shown in Fig. 7. The nondimensional frequency parameter λ is defined as

$$\lambda = \omega A^2/\sqrt{\rho_s H/D}, \tag{49}$$

where $D = EH^3/[12(1-v^2)]$ is the plate flexural rigidity, and ω is the vibrational frequency. Five different types of continuum solid elements were tested: 8-node linear brick (C3D8), 8-node linear brick with reduced integration with hourglass control (C3D8R), 8-node linear brick with incompatible modes (C3D8I), 20-node quadratic brick (C3D20), and 20-node quadratic brick with reduced integration (C3D20R). One layer of 10×10 elements were employed. As expected, 8-node linear brick (C3D8) and 8-node linear brick with reduced integration (C3D8R) elements failed to capture the measured frequencies due to shear locking and hourglass problems, respectively. The predicted frequencies compared well with experimental measurements for the other elements (C3D8I, C3D20, and C3D20R).

To model general propeller geometries, triangular elements are needed to model sharp edges at the blade tip and edges. Since first-order triangular elements tend to be overly stiff and exhibit slow convergence with mesh refinement, the use of second-order elements is recommended for general propeller blade geometries. In particular, 20-node quadratic brick elements with reduced integration (C3D20R) appears to be the optimum in terms of numerical accuracy and computational effort.

To investigate the sensitivity of the solution to varying mesh size, comparison of the predicted and measured frequencies for different arrangements of $l \times m \times n$ (spanwise×chordwise×through thickness) C3D20R elements are shown in Fig. 8. As indicated in the figure, the solution is not sensitive to the mesh size. One layer of elements through the thickness is sufficient to capture the modal frequencies for the twisted cantilever plate in the case of lower order modes than five.

4.2. Elliptic hydrofoil

To validate the hydroelastic modelling, numerical results for an elliptic hydrofoil are compared with analytical solution obtained using the 2-D added mass coefficient. For a rectangular hydrofoil with an elliptic cross-section at zero angle of attack ($\alpha = 0°$), the 3-D added mass coefficients can be approximated by applying strip theory. Denoting the radius of the major and minor axis as a and b, respectively, the 2-D added mass coefficients based on potential theory

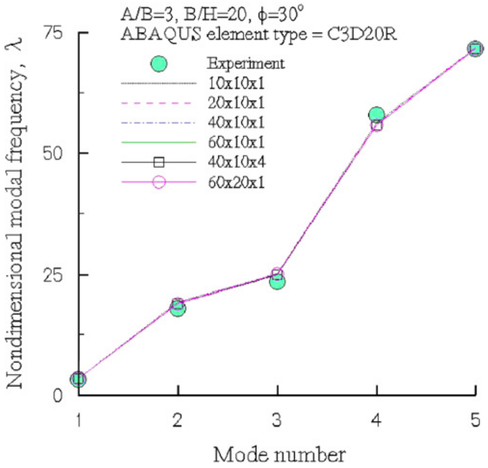

Fig. 8. Comparisons of the predicted and measured frequency parameter for different mesh arrangements of $l \times m \times n$ (spanwise×chordwise×through thickness) C3D20R elements.

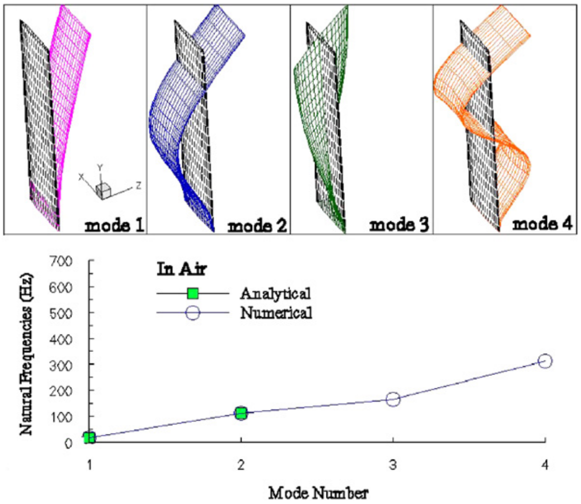

Fig. 9. Top: Predicted mode shapes for a cantilever elliptic hydrofoil *in air*. Bottom: Comparison of the predicted natural frequencies with analytical values obtained using the Timoshenko beam theory; 20 × 20 C3D20R elements.

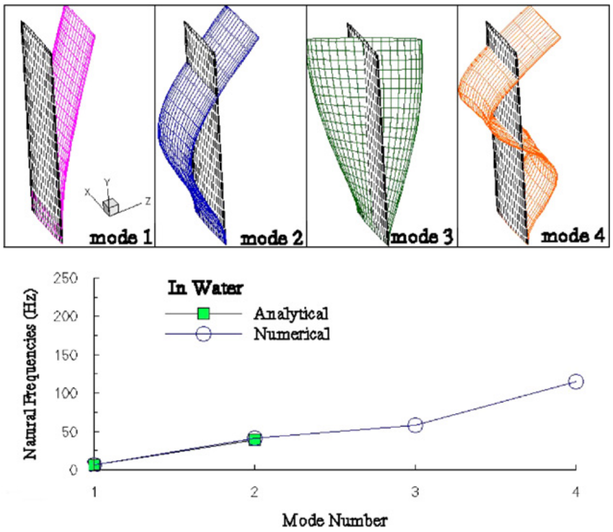

Fig. 10. Top: Predicted mode shapes for a cantilever elliptic hydrofoil *in water*. Bottom: Comparison of the predicted natural frequencies with analytical values obtained using the Timoshenko beam theory and the 2-D added mass coefficients; 20 × 20 C3D20R elements were used in the numerical analysis.

are given by Eq. (50) (Newman, 1997):

$$m_{11} = \pi\rho b^2, \quad m_{22} = \pi\rho a^2, \quad m_{66} = \pi\rho(a^2 - b^2)^2/8. \tag{50}$$

The geometric parameters of the test hydrofoil are as follows: L (span) $= 0.5\,\mathrm{m}$, $C = 2a$ (chord) $= 0.125\,\mathrm{m}$, $T = 2b$ (maximum thickness) $= 0.00625\,\mathrm{m}$. The material properties are: ρ (fluid density) $= 1000\,\mathrm{kg/m^3}$, ρ_s (solid density) $= 2800\,\mathrm{kg/m^3}$, E (Young' s modulus) $= 72\,\mathrm{GPa}$, ν (Poisson' s ratio) $= 0.3$. The effect of damping is ignored in this validation study. Based on the Timoshenko beam theory, the natural frequencies of an uniform cantilever beam *in air* can be computed as follows (Chopra, 2001):

$$\omega_n^{\mathrm{air}} = \left(\frac{a_n}{L^2}\sqrt{\frac{EI_{11}}{\rho_s A}}\right)\frac{1}{\sqrt{1 + (n\pi r/L)^2(1 + E/kG)}}, \tag{51}$$

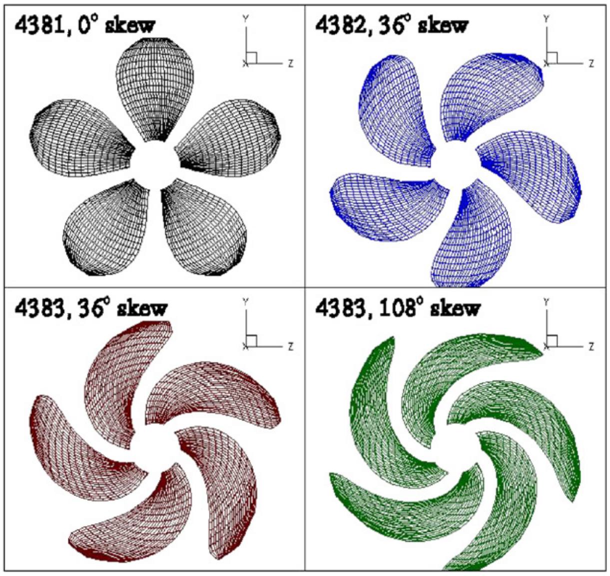

Fig. 11. BEM representation of propeller 4381, 4382, 4383, and 4384.

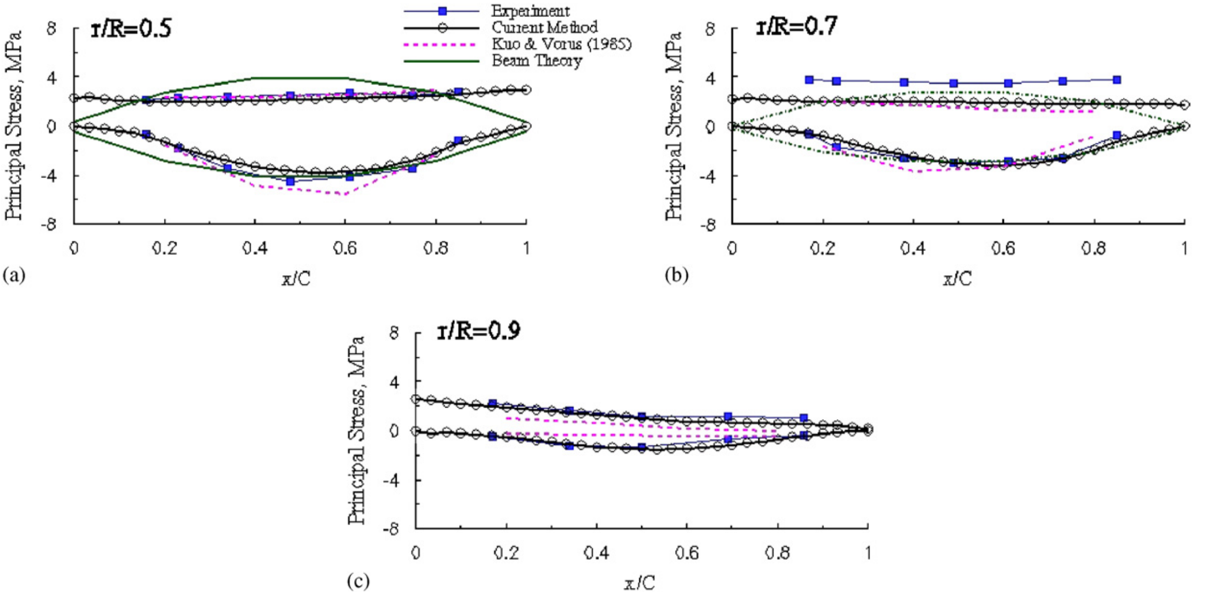

Fig. 12. Comparison of the predicted versus measured principal stresses for propeller 4383 subjected to an uniform pressure of 6895 Pa (1 psi) on the face side.

where n is the mode number, $a_1 = 3.516$, $a_2 = 22.03$, $a_3 = 61.70$, and $a_4 = 120.9$. $A = \pi ab$, $I_{11} = \pi ab^3/4$, $r = \sqrt{I_{11}/A}$, and $k = \frac{4}{3}$.

If the beam is in water, then the 2-D added mass should be superimposed on the material mass. Thus, the natural frequencies *in water* are given by

$$\omega_n^{\text{water}} = \left(\frac{a_n}{L^2}\sqrt{\frac{EI_{11}}{\rho_s A + \pi\rho a^2}}\right)\frac{1}{\sqrt{1+(n\pi r/L)^2(1+E/kG)}}. \qquad (52)$$

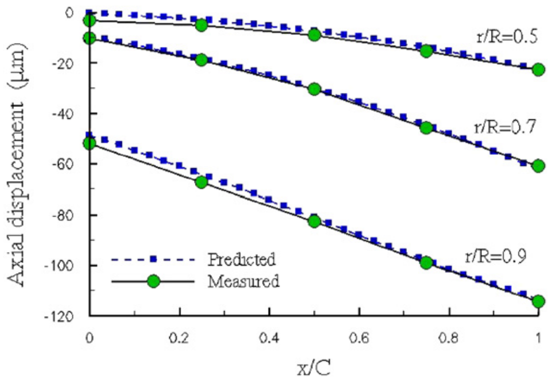

Fig. 13. Comparison of the predicted versus measured blade deflection for propeller 4383 subjected to an uniform pressure of 6895 Pa (1 psi) on the face side.

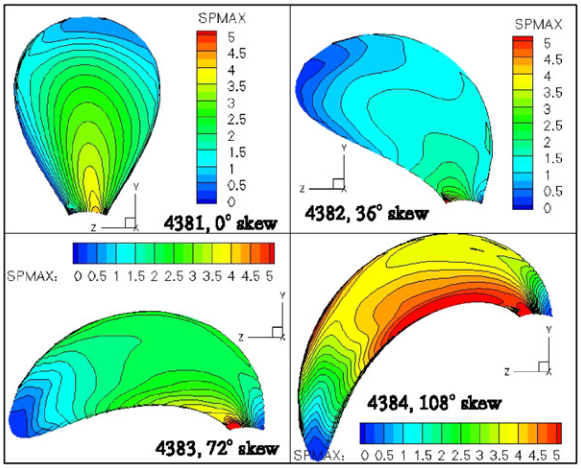

Fig. 14. Comparison of the predicted maximum principal stress contours (in MPa) for all four propellers.

Using the coupled BEM/FEM method presented in this paper, the predicted mode shapes and natural frequencies of the elliptic hydrofoil in air and in water are shown in Figs. 9 and 10, respectively. As expected, the mode shapes are very similar in air and in water, and the natural frequencies are reduced by approximately 65% in water due to the effect of the added mass. Also shown in Figs. 9 and 10 are the analytical natural frequencies given by Eqs. (51) and (52). The agreement between the numerical and analytical frequencies is excellent for the first two modes. For modes higher than two, Eqs. (51) and (52) are not valid due to inability of the beam theory to account for twisting of the foil.

4.3. Highly skewed propellers

The next validation test is for a series of four five-bladed skewed marine propellers. The propellers represent typical designs for container ships or single-screw destroyer-type ships. The parent propeller has a symmetric blade outline with zero skew, and the other three propellers have maximum skew angles (measured in the plane of the propeller disk) of 36°, 72°, and 108° (Boswell, 1971). The geometric parameters for all four propellers were the same except skew, pitch, and camber. The propellers were required to achieve equal open water performance, which was achieved by varying the propeller pitch and camber. The propeller geometries are given in Boswell (1971) and Cumming et al. (1972), and are shown in Fig. 11. The propellers were subjected to an uniform static air pressure of 6895 Pa (1 psi) on the face (pressure) side. The tests were conducted on a 0.3048 m (1 ft) model ($\frac{1}{23}$-scale) constructed of 2014-T4 aluminum in a specially designed pressure chamber. Systematic stress measurements for all the propellers in this series are given in Boswell et al.

(1976), and the accuracy of the measurements was estimated to be within ±5% (Boswell et al., 1976). Deflection measurements of the 72°-skew model (propeller 4383) via holographic techniques were presented in Dhir and Sikora (1971).

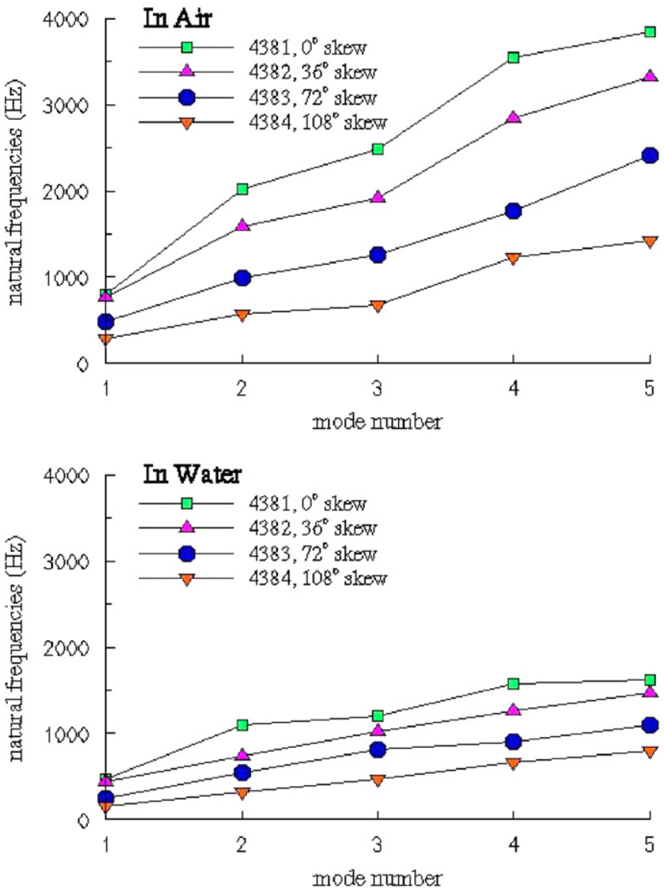

Fig. 15. Predicted natural frequencies of propellers 4381, 4382, 4383, and 4384 in air (top) and in water (bottom).

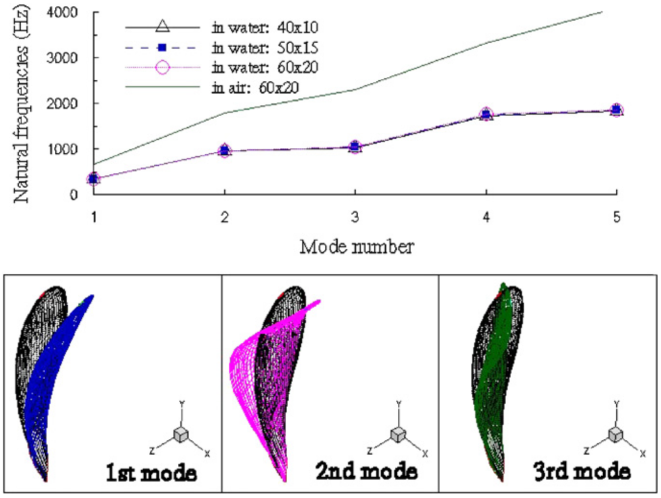

Fig. 16. Convergence of natural frequencies with mesh size. Propeller 4148; $NC \times MR$ BEM panels, $E = 75\,\mathrm{GPa}$.

Examples of the comparison between predicted and measured principal stresses and deflections for propeller 4383 (72° skew) are shown in Figs. 12 and 13, respectively. Also shown in Fig. 12 are the predicted stresses obtained by Kuo and Vorus (1985) using FEM and by Boswell et al. (1976) using beam theory. As shown in the figures, the predicted

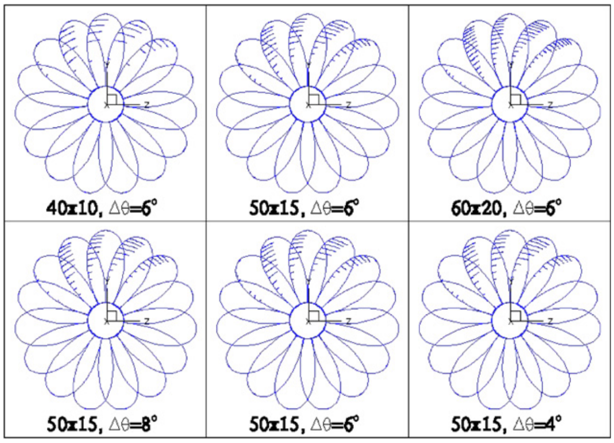

Fig. 17. Convergence of cavitation pattern with mesh size and time step size. Propeller 4148; $NC \times MR$ BEM panels, $E = 75\,\text{GPa}$.

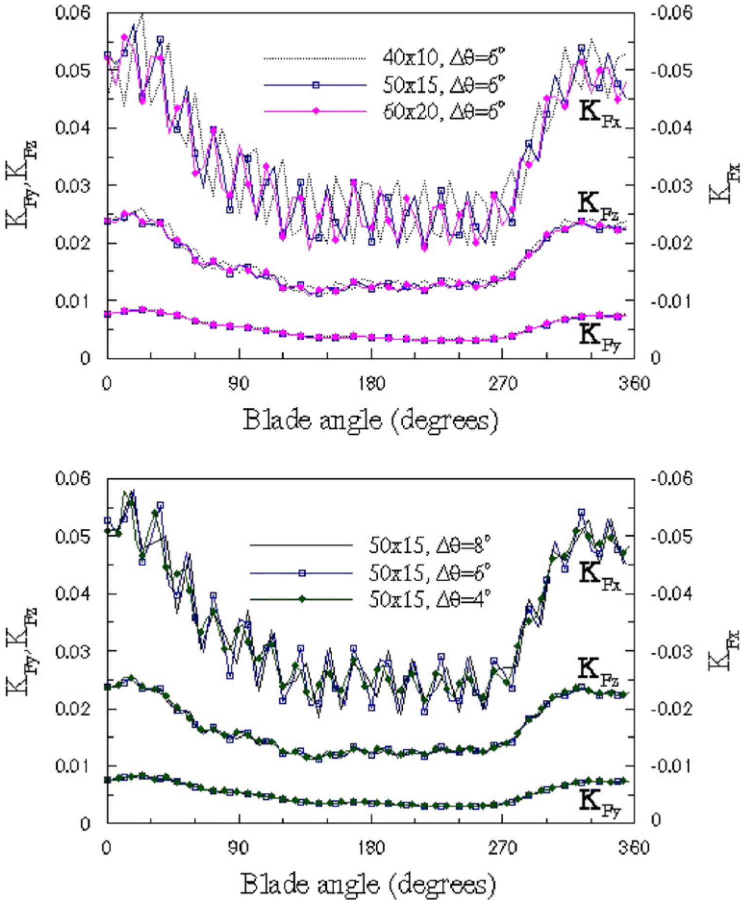

Fig. 18. Convergence of total hydrodynamic load coefficients (per blade) with mesh size and time step size. Propeller 4148; $E = 75\,\text{GPa}$.

stresses and deflections compared well with experimental measurements and with the numerical results obtained by Kuo and Vorus (1985). The results also indicate that the modified beam theory is not able to capture the stress distribution for highly skewed propellers. Comparison of the predicted maximum principal stress contours (in ksi) for all four propellers are shown in Fig. 14. As expected, the maximum stress levels increased with increasing skew. In addition, as the skew angle increases, the maximum principal stress moves toward the trailing edge at the inner radii and towards the leading edge at the outer radii, which agreed with experimental measurements presented in Boswell et al. (1976).

The predicted natural frequencies of the propellers in air and in water are shown in Fig. 15. As indicated in the figure, the natural frequencies decreased substantially in water due to the added mass effect. In addition, the natural frequencies decreased with increasing in skew due to increase in blade flexibility. The numerical prediction using the present method for all four propellers were generated using one layer of 60 × 36 quadratic solid elements (C3D20R and C3D15). The assigned material properties are as follows: ρ (fluid density) $= 1000\,\mathrm{kg/m^3}$, ρ_s (solid density) $= 2800\,\mathrm{kg/m^3}$, E (Young' s modulus) $= 75\,\mathrm{GPa}$, and v (Poisson' s ratio) $= 0.33$.

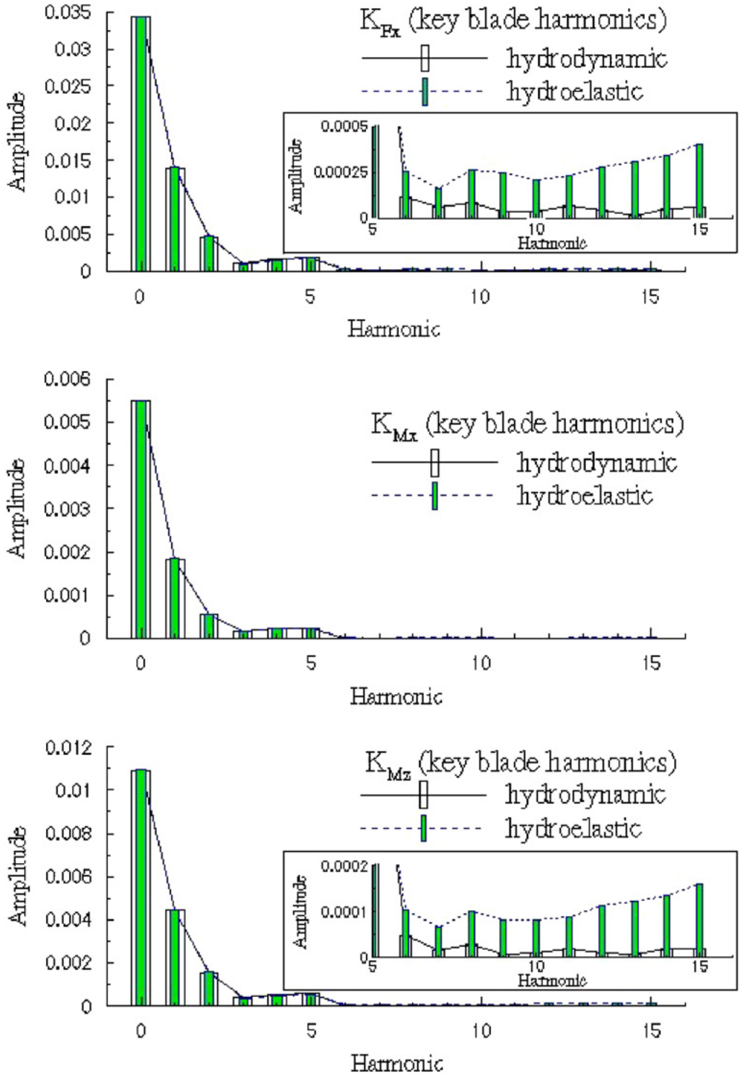

Fig. 19. Comparison of the rigid blade and elastic blade cavitating force harmonics (per blade) for $E = 75\,\mathrm{GPa}$. Propeller 4148; $50(NC) \times 15(MR)$ BEM panels, $\Delta\theta = 6^\circ$, $E = 75\,\mathrm{GPa}$.

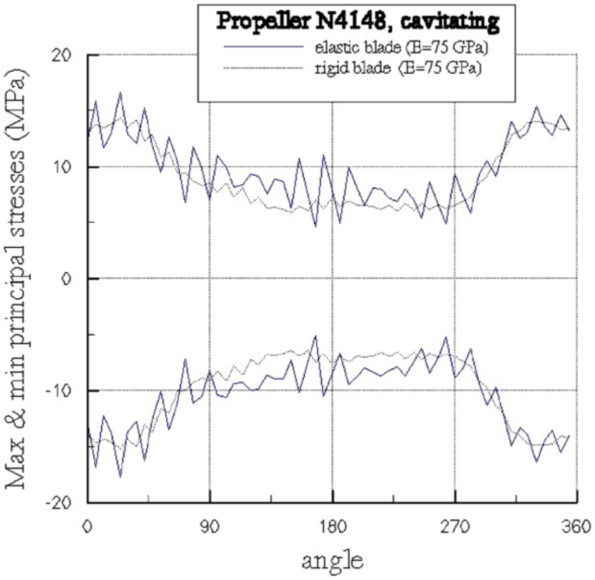

Fig. 20. Comparison of the maximum and minimum principal stresses for the rigid blade and elastic blade. Propeller 4148; $25(NC/2)\times 15(MR)$ FEM brick elements, $\Delta\theta = 6^{\circ}$.

5. Unsteady hydroelastic analysis of a cavitating propeller

The presented coupled BEM/FEM method is applied to investigate the dynamic performance of propeller 4148 in nonaxisymmetric, cavitating flow. The geometry, inflow wake, flow conditions, predicted rigid-blade hydrodynamic performance, and comparison of the predicted and observed cavitation patterns have already been presented in Section 3.2. The unsteady hydrodynamic forces, blade stress, and deflections were not measured in the experiment. Thus, only numerical predictions are shown in this section. The propeller diameter is 304.8 mm (1 ft), and the propeller angular velocity is 1050 rpm. The assigned material properties are as follows: ρ (fluid density) $= 1000\,\mathrm{kg/m^3}$, ρ_s (solid density) $= 2800\,\mathrm{kg/m^3}$, E (Young' s modulus) $= 75\,\mathrm{GPa}$, and v (Poisson' s ratio) $= 0.33$. The structural damping is assumed to be negligible compared to the hydrodynamic damping. Thus, the total damping matrix is the same as the hydrodynamic damping matrix. The predicted natural frequencies in air and in water are shown in Fig. 16 along with the predicted wetted mode shapes. The reduction in natural frequencies due to added-mass effect was approximately 50% for all the modes. Also shown in Fig. 16 is the convergence of the natural frequencies in water with number of BEM panels.[2] The convergence of the unsteady cavitation patterns and total hydrodynamic load coefficients ($F_{\mathrm{tot}}(t) = F(t) + f(t)$) per blade with varying grid size and time step size (via blade angle increment $\Delta\theta$) are shown in Figs. 17 and 18, respectively.K_{F_x}, K_{F_y}, and K_{F_z} denote the x, y, and z components of the per blade force coefficients nondimensionalized by $\rho n^2 D^4$. K_{M_x}, K_{M_y}, and K_{M_z} denote the x, y, and z components of the per blade moment coefficients nondimensionalized by $\rho n^2 D^5$. The variables n and D denote the propeller rotational frequency and diameter, respectively.

As shown in the figures, the numerical solution converged with space and time discretizations. Comparison of the rigid-blade and elastic blade force harmonics and the time-history of the maximum principal stresses are shown in Figs. 19 and 20, respectively. The fundamental natural frequency of propeller 4148 in water is 343 Hz, which corresponds to the 20th harmonic of the propeller angular velocity (1050 rpm or 17.5 Hz). Thus, only small amplifications of the higher harmonics are expected for K_{F_x} and K_{M_z} since the first mode is bending about the z-axis. As shown in Figs. 19 and 20, this behavior is correctly predicted by the current method.

To demonstrate the effect of resonance, the Young's modulus, E, of the material was reduced to 15 GPa, while all other input parameters were kept constant. Due to the increase in material flexibility, the blade's fundamental natural frequency in water is reduced to 151.5 Hz, which corresponds to the ninth harmonic of the propeller angular velocity.

---

[2] $NC \times MR$ (chordwise by spanwise) BEM surface panels is equivalent to $NC/2 \times MR$ (chordwise by spanwise) volumetric FEM elements.

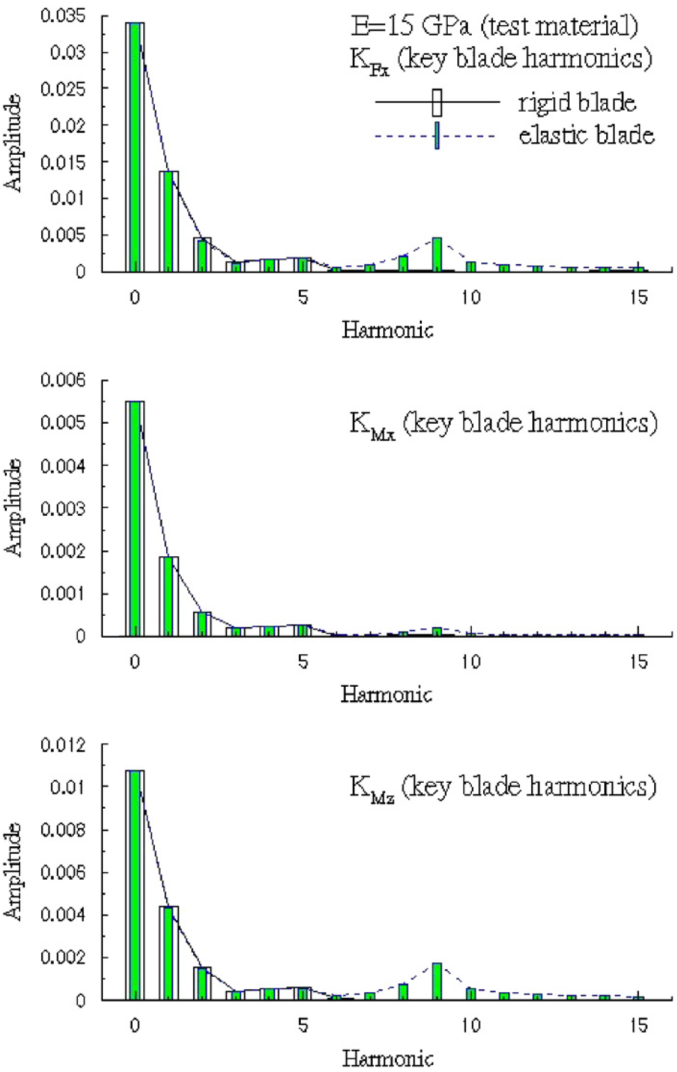

Fig. 21. Comparison of the rigid blade and elastic blade cavitating force harmonics (per blade) for $E = 15\,\mathrm{GPa}$. Propeller 4148; $50(NC) \times 15(MR)$ BEM panels, $\Delta\theta = 6°$.

The resulting total hydrodynamic load coefficients ($F_{\mathrm{tot}}(t) = F(t) + f(t)$) per blade are compared with the rigid-blade hydrodynamic load coefficients in Fig. 21. As expected, the load coefficients around the ninth harmonic are amplified. Comparison of the blade tip displacements at the trailing edge for $E = 75\,\mathrm{GPa}$ (aluminum) and $E = 15\,\mathrm{GPa}$ (test material) is shown in Fig. 22. As expected, the displacements are significantly amplified for $E = 15\,\mathrm{GPa}$. In addition, there are 20 oscillations per revolution for $E = 75\,\mathrm{GPa}$ and nine oscillations per revolution for $E = 15\,\mathrm{GPa}$, which confirms that the oscillations are due to blade vibration corresponding to the first mode in water.

6. Conclusion

A 3-D potential-based BEM has been coupled with a 3-D FEM for the time-dependent hydroelastic analysis of cavitating propulsors. The BEM is applied to evaluate the moving cavity boundaries and corresponding hydrodynamic forces, as well as the added mass and hydrodynamic damping matrices. The FEM is applied to analyze the structural deformations and stress distributions due the applied hydrodynamic and centrifugal loads. The added mass and

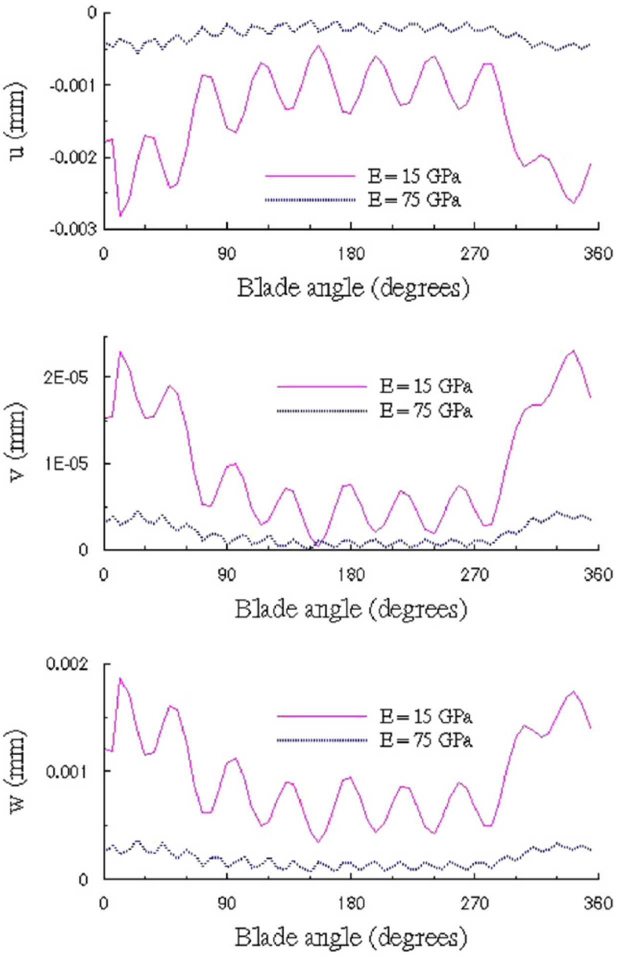

Fig. 22. Comparison of the blade tip displacements at the trailing edge for $E = 75$ and 15 GPa. Propeller 4148; $50(NC) \times 15(MR)$ BEM panels, $\Delta\theta = 6°$; u, v, and w denote the displacements in the x, y, and z directions, respectively.

hydrodynamic damping matrices are superimposed onto the structural mass and damping matrices, respectively, to account for the change in hydrodynamic pressure and blade motion due to fluid–structure interaction. The problem is solved in the time-domain using an implicit time integration scheme. The formulation for both BEM and FEM has been presented, along with the hydroelastic coupling algorithm. The predicted hydrodynamic forces and cavitation patterns compared well with experimental measurements and observations. Systematic experimental validation studies showed excellent agreement between the predicted and measured natural frequencies, stress distributions, and blade displacements. The predicted hydroelastic response of propeller 4148 in unsteady, cavitating flow seemed reasonable, and the results converged with grid size and time step size. Based on the results, the following conclusions can be drawn:

(1) Quadratic continuum elements are recommended for the finite element modelling of propeller-like geometries. Linear elements are not suitable due to shear locking and hourglass problems.
(2) The modified beam theory will not be able to accurately capture the stress distribution of complex propeller geometries (e.g. blades with wide outline, high skew, vastly asymmetrical blade sections, etc.) due to the oversimplifications involved. In addition, the beam theory will not be able to capture the higher mode dynamics due to its inability to model the twisting of the blades.
(3) The maximum stress levels increased with increasing skew, and the location of the maximum stress moves toward the trailing edge at the inner radii and toward the leading edge at the outer radii for highly skewed propellers.

(4) The blade natural frequencies decreased with increased skew due to increase in blade flexibility.
(5) The blade natural frequencies decreased in water due to added mass effects. The decrease in fundamental frequency may cause the blades to resonate at lower harmonics, which will increase the magnitude and period of the oscillations of the hydrodynamic blade forces, stresses, and displacements.

Although the present method compared well with experimental measurements for metallic propellers and converged quickly with grid size and time step size, additional work is still needed to account for change in hydrodynamic load due to blade deformation. For moderate to very flexible propellers (e.g. composite propellers), substantial blade deformations will occur (i.e. severe change in pitch, skew, and rake distributions), which will in turn affect the hydrodynamic performance and cavitation patterns. Work is currently underway to extend the present method for fully nonlinear hydroelastic analysis of cavitating propellers in steady and unsteady flow conditions.

Acknowledgment

Support for this research was provided by Naval Surface Warfare Center Carderock Division (Contract Number N000167-05-M-0100) and Office of Naval Research (Contract Number N00014-05-1-0694).

References

ABAQUS, I., 2004. ABAQUS Version 6.5 Documentation. ABAQUS, Inc., 1080 Main Street, Pawtucket, RI 02860, USA.

Atkinson, P., 1968. On the choice of method for the calculation of stress in marine propellers. Transactions, Royal Institution of Naval Architecture 110, 447–463.

Atkinson, P., 1973. The prediction of marine propeller distortion and stresses using a super-parametric thick shell finite-element model. Transactions, Royal Institution of Naval Architecture 115, 359–375.

Atkinson, P., Glover, J., 1988. Propeller hydroelastic effects. Transactions, Society of Naval Architects and Marine Engineers 21.

Boswell, R., 1971. Design, cavitation performance and open-water performance of a series of research skewed propellers. Technical Report 3339, DTNSRDC.

Boswell, R., Miller, M., Kader, R., 1976. Static stress measurements on a series of skewed propeller blades with and without forward rake. Technical Report SPD-712-01, David Taylor Model Basin, USA.

Brillouin, M., 1911. Les surfaces de glissement de Helmholtz et la resistance des fluides. Annales de Chimie and de Physique 23, 145–230.

Choi, J., 2000. Vortical inflow—propeller interaction using unsteady three-dimensional euler solver. Ph.D. Thesis, Department of Civil Engineering, The University of Texas at Austin.

Chopra, A., 2001. Dynamics of Structures, second ed. Prentice-Hall, Englewood Cliffs, NJ.

Conolly, J., 1961. Strength of propellers. Transactions, Royal Institution of Naval Architecture 103, 139–204.

Cumming, R.A., Morgan, W.B., Boswell, R.J., 1972. Highly skewed propellers. Transactions, Society of Naval Architects and Marine Engineers 80, 98–135.

Dhir, S., Sikora, J., 1971. Holographic displacement measurements on a highly skewed propeller blade. Technical Report 3680, Department of the Navy, Naval Ship Research and Development Center, Bethesda, MD, USA.

Dyson, P.K., 2000. The modelling, testing and design, of a surface piercing propeller drive. Ph.D. Thesis, Department of Mechanical and Marine Engineering, Plymouth University, UK.

Dyson, P.K., Chudley, J., Grieve, D., 2000. An experimental programme to determine the mean and time varying loads imposed by surface piercing propellers. In: Sea Australia 2000, Sydney.

Fine, N., Kinnas, S., 1993. A boundary element method for the analysis of the flow around 3-d cavitating hydrofoils. Journal of Ship Research 37, 213–224.

Fine, N.E., 1992. Nonlinear analysis of cavitating propellers in nonuniform flow. Ph.D. Thesis, Department of Ocean Engineering, Massachusetts Institute of Technology, USA.

Genalis, P., 1970. Elastic strength of propellers—an analysis by matrix methods. Technical Report 3397, David Taylor Research Center.

Greeley, D., Kerwin, J., 1982. Numerical methods for propeller design and analysis in steady flow. Society of Naval Architects and Marine Engineers Transactions 90, 415–453.

Hess, J.L., Valarezo, W., 1985. Calculation of steady flow about propellers by means of a surface panel method. In: 23rd Aerospace Sciences Meeting. AIAA, Reno, Nevada, pp. 1–8.

Hsin, C.-Y., 1990. Development and analysis of panel method for propellers in unsteady flow. Ph.D. Thesis, Department of Ocean Engineering, Massachusetts Institute of Technology, USA.

Kerwin, J., Lee, C.-S., 1978. Prediction of steady and unsteady marine propeller performance by numerical lifting-surface theory. Transactions Society of Naval Architects and Marine Engineers 86, 218–253.

Kerwin, J., Kinnas, S., Lee, J.-T., Shih, W.-Z., 1987. A surface panel method for the hydrodynamic analysis of ducted propellers. Transactions Society of Naval Architects and Marine Engineers 95, 93–122.

Kielb, R., Leissa, A., MacBain, J., 1985. Vibrations of twisted cantilever plates—a comparison of theoretical results. International Journal for Numerical Methods in Engineering 21, 1365–1380.

Kinnas, S., Fine, N., 1989. Theoretical prediction of the midchord and face unsteady propeller sheet cavitation. In: Proceedings of the Fifth International Conference on Numerical Ship Hydrodynamics, Hiroshima, Japan.

Kinnas, S., Fine, N., 1991. Non-linear analysis of the flow around partially or super-cavitating hydrofoils by a potential based panel method. In: Boundary Integral Methods—Theory and Applications, Proceedings of the IABEM-90 Symposium, Rome, Italy, October 15–19, 1990. Springer, Heidelberg, pp. 289–300.

Kinnas, S., Fine, N., 1992. A nonlinear boundary element method for the analysis of unsteady propeller sheet cavitation. In: Nineteenth Symposium on Naval Hydrodynamics, Seoul, Korea, pp. 717–737.

Kinnas, S., Fine, N., 1993. A numerical nonlinear analysis of the flow around two- and three-dimensional partially cavitating hydrofoils. Journal of Fluid Mechanics 254, 151–181.

Kinnas, S., Hsin, C.-Y., 1992. A boundary element method for the analysis of the unsteady flow around extreme propeller geometries. AIAA Journal 30 (3), 688–696.

Kinnas, S., Pyo, S., 1999. Cavitating propeller analysis including the effects of wake alignment. Journal of Ship Research 43 (1), 38–47.

Kinnas, S., Young, Y., 2003. Modeling of cavitating or ventilated flows using bem. International Journal of Numerical Methods for Heat & Fluid Flow 13 (6), 672–697.

Kinnas, S., Choi, J., Lee, H., Young, J., 2000. Numerical cavitation tunnel. In: NCT50, International Conference on Propeller Cavitation. Newcastle-upon-Tyne, England, pp. 137–157.

Kinnas, S., Lee, H., Young, Y., 2003a. Modeling of unsteady sheet cavitation on marine propulsors. International Journal of Rotating Machinery 9 (4), 263–277.

Kinnas, S., Young, Y., Lee, H., Gu, H., Natarajan, S., 2003b. Prediction of cavitating flow around single or two-component propulsors, ducted propellers, and rudders. In: RINA CFD 2003: CFD Technology in Ship Hydrodynamics Conference, London, UK.

Kuo, J., 1984. Analysis of propeller blade dynamic stresses. Ph.D. Thesis, Department of Naval Architecture and Marine Engineering, The University of Michigan, Ann Arbor, MI, USA.

Kuo, J., Vorus, W., 1985. Propeller blade dynamic stress. In: Tenth Ship Technology and Research (STAR) Symposium. Norfolk, VA, pp. 39–69.

Lee, H., Gu, H., Kakar, K., Kinnas, S., 2001. MPUF-3A (version 2.0) user's manual and documentation. Technical Report 01-5, Ocean Engineering Group, University of Texas at Austin, USA.

Lee, J.-T., 1987a. A potential based panel method for the analysis of marine propellers in steady flow. Ph.D. Thesis, Department of Ocean Engineering, Massachusetts Institute of Technology, USA.

Lee, J.-T., 1987b. A potential based panel method for the analysis of marine propellers in steady flow. Ph.D. Thesis, Department of Ocean Engineering, Massachusetts Institute of Technology, USA.

Lin, H., Lin, J., 1996. Nonlinear hydroelastic behavior of propellers using a finite element method and lifting surface theory. Journal of Marine Science and Technology 1 (2), 114–124.

Ma, J., 1974. Stresses in marine propellers. Journal of Ship Research 18 (4), 252.

MacBain, J., Kielb, R., Leissa, A., 1985. Vibrations of twisted cantilever plates—experimental investigation. Journal of Engineering for Gas Turbines and Power 107, 187–196.

Mishima, S., Kinnas, S., Egnor, D., 1995. The CAvitating PRopeller EXperiment (CAPREX), Phases I & II. Technical Report, Department of Ocean Engineering, Massachusetts Institute of Technology, USA.

Morgan, W., 1954. An approximate method of obtaining stress in a propeller blade. Technical Report 919, David Taylor Research Center, USA.

Morino, L., Kuo, C.-C., 1974. Subsonic potential aerodynamic for complex configurations: a general theory. AIAA Journal 12 (2), 191–197.

Mueller, A., Kinnas, S., 1999. Propeller sheet cavitation predictions using a panel method. ASME Journal of Fluids Engineering 121, 282–288.

Newman, J., 1997. Marine Hydrodynamics. The MIT Press, Cambridge, MA.

Schoenherr, K., 1963. Formulation of propeller blade strength. In: Spring Meeting, The Society of Naval Architects and Marine Engineers, New Orleans, LA, USA.

Sontvedt, T., 1974. Propeller blade stresses, application of finite element methods. Computers and Structures 4, 193–204.

Tabbara, M., Blacker, T., Belytschko, T., 1994. Finite element derivative recovery by moving least squares interpolants. Computational Methods in Applied Mechanical Engineering 117, 211–223.

Taylor, D., 1933. The speed and power of ships. Technical Report, U.S. Government Printing Office, Washington, DC.

Villat, H., 1914. Sur la validité des solutions de certain problem d' hydrodynamique. Journal de Mathematiques 6 (10), 231–290.

Vorus, W., 1981. Hydrodynamic added-mass matrix of vibrating ship based on a distribution of hull surface sources. SNAME Transactions 89, 397–416.

Young, Y., Kinnas, S., 2001a. A BEM for the prediction of unsteady midchord face and/or back propeller cavitation. ASME Journal of Fluids Engineering 123, 311–319.

Young, Y., Kinnas, S., 2001b. Numerical modeling of supercavitating and surface-piercing propeller flows. In: CAV 2001: Fourth International Symposium on Cavitation. California Institute of Technology, Pasadena, CA, USA.

Young, Y., Kinnas, S., 2003a. Analysis of supercavitating and surface-piercing propeller flows via bem. Journal of Computational Mechanics 32 (5–6), 269–280.

Young, Y., Kinnas, S., 2003b. Numerical analysis of surface-piercing propellers. In: 2003 Propeller and Shaft Symposium. Society of Naval Architects and Marine Engineers, Virginia Beach, VA, pp. 4-1–4-20.

Young, Y., Kinnas, S., 2003c. Numerical modeling of supercavitating propeller flows. Journal of Ship Research 47 (1), 48–62.

Young, Y., Kinnas, S., 2004. Performance prediction of surface-piercing propellers. Journal of Ship Research 48 (4).